Available online at www.sciencedirect.com
ScienceDirect
Comput. Methods Appl. Mech. Engrg. 00 (2023) 1–28
Computer methods in applied mechanics and engineering

Proper orthogonal decomposition assisted eigendeformation-based mathematical homogenization method for modeling cracks in 3D polycrystalline microstructures

Damin Xia[a], Caglar Oskay[a,*]

[a]*Department of Civil and Environmental Engineering, Vanderbilt University, Nashville, TN 37235, United States of America*

Abstract

In this manuscript, a reduced order model (ROM) is proposed for full three-dimensional (3D) polycrystalline microstructures with tortuous short cracks. The model reformulates eigendeformation-based homogenization method (EHM) assisted with the proper orthogonal decomposition (POD) method to account for local plastic deformation and crack separation fields. A constrained optimization problem is formulated with reduced order objective functions and un-reduced constraints to solve for the separation. To make the optimization process more feasible, an integrated form of the constraint is introduced, enabling the use of only one constraint regardless of the crack morphology. The model is verified against direct numerical simulations (DNS) with crystal plasticity as the constitutive relation. The use of priori knowledge in building crack separation field basis functions as well as sampling strategies in the absence of prior knowledge are discussed. The performance and accuracy of the ROM are assessed under various loading conditions and different crack configurations.

Keywords: Computational homogenization; Proper orthogonal decomposition; Reduced order modeling; Tortuous short cracks; Crystal plasticity

1. Introduction

Microstructurally short cracks (MSCs) occur in polycrystalline materials as manufacturing process- or loading process-induced defects. They are the cause of the onset of failure under a range of loading conditions including high cycle fatigue. A crack is identified as an MSC if the length scale of the crack is comparable to the microstructural parameters such as the grain size [1–3]. Depending on the underlying microstructure, the size of an MSC ranges from a few microns to hundreds of microns [4]. Therefore, the behavior of MSCs is significantly influenced by local texture characteristics such as grain orientations, subgrains, and grain boundaries. This influence may cause the MSCs to propagate through the microstructure in a highly tortuous path [5–10].

The Crystal Plasticity Finite Element (CPFE) method [11, 12] is one of the most flexible full-field schemes that can be used to explicitly incorporate cracks into the microstructure and account for the presence and growth of MSCs. Crystal plasticity modeling is used to capture the constitutive behavior within individual grains, while explicit discretization of the polycrystalline microstructure connects the response of individual grains to the overall mechanical response of the microstructure volume [13–16]. The CPFE method has been integrated with the adaptive crack insertion technique [9, 17–24], the phase field method (PFM) [25–32], the extended finite element method (XFEM) [33–44], cohesive zone modeling (CZM) [45, 46], and the node release method [47] to study response fields around MSCs

*Correspondence to: VU Station B#351831, 2301 Vanderbilt Place, Nashville, TN 37235, United States of America.
Email address: caglar.oskay@vanderbilt.edu (Caglar Oskay)

and short crack propagation behavior. Of the aforementioned methods, the CZM and the node release method typically require a prescribed crack path, which can be a limitation for polycrystalline materials as the crack path is typically highly uncertain due to texture-crack interactions. XFEM utilizes enrichment functions to account for the presence of cracks, thereby eliminating the need for mesh conformity. Despite its advantages, most studies on polycrystalline materials utilizing XFEM have been restricted to modeling 2D structures, and only limited progress has been made in using XFEM to model cracks in fully 3D polycrystalline microstructures [42]. On the other hand, the PFM, due to its flexibility in modeling complex crack configurations, has gained significant attention in recent years. Its independence from finite element mesh geometry further contributes to its appeal. Despite efforts to enhance the efficiency of this approach [29], its application to fatigue prediction is still restricted by high computational costs because of the requirement of a mesh fine enough to resolve the phase-field length scale.

Adaptive crack insertion employs remeshing to conform the crack morphology within the underlying volume mesh, and it is a classical method to explicitly consider the influence of cracks. This approach has been used to incorporate complex and tortuous crack morphologies in 3D microstructures [9]. However, during a crack propagation process, the need for high resolution around the crack front and the requirement of constantly remeshing incur significant computational expense. Proudhon *et* al. [9] used an experimentally measured 3D microstructure consisting of several hundred grains to model short crack propagation. It is reported that each step of crack growth takes approximately 3-5 days to compute. The majority of the computational resources are spent to executing the CPFE code to evaluate the response of the microstructure with crack subjected to a single load cycle, with the remaining procedures such as remeshing and post-processing taking up smaller fraction of the total simulation time.

The Fast Fourier Transform (FFT) method is another full-field modeling approach, which has been shown to offer significant computational efficiency compared to the CPFE method [48]. Rovinelli *et* al. [49] recently compared the response fields near a crack tip using the FFT and CPFE methods in conjunction with crack insertion, and found that the FFT method predicts comparable response fields to CPFE while providing improved computational efficiency. FFT is also combined with PFM to model short cracks [50, 51], where cracks of complex morphologies can be represented in a polycrystalline microstructure. The application of FFT method for short crack modeling remains limited due to constraints in boundary conditions, the need for a uniform grid that constrains the crack morphology, and the occurrence of Gibbs' oscillations [49, 52].

Reduced-order modeling (ROM) schemes can significantly alleviate the computational costs as compared to full-field methods. The literature on ROMs for polycrystalline microstructures with MSCs is scarce at best, whereas a few approaches have been proposed for composite materials.

Oliver *et* al. [53] proposed a hyperreduction model to simulate composite fracture, where the material failure is modeled for both micro- and macro-scales through continuum strong discontinuity approach [54]. The microscale simulations were accelerated by the use of proper orthogonal decomposition (POD). In a recent study, Liu [55] proposed a new method for analyzing debonding in unidirectional fiber-reinforced composites using deep material networks (DMNs) enhanced with cohesive layers. Eigendeformation-based reduced-order homogenization model (EHM) is a ROM approach that offers a hierarchical strategy for reducing the complexity of modeling heterogeneous materials [56–58]. EHM has been extended to account for the presence of plasticity [59–61] and both continuum and discrete interfacial damage [62, 63]. More recently, Brandyberry *et* al. [64] implemented an interface-enriched generalized finite element method version of EHM to study interface damage. Xia *et* al. [65] advanced the EHM for polycrystalline materials with microstructurally short cracks in the context of quasi-2D microstructures. This approach accounts for straight or kinked cracks, in which the stress and strain concentrations around the crack tips are captured by locally refining the reduced order basis. The aforementioned models considered pre-defined and/or simple crack morphologies (e.g., bounded by the interfaces between matrix and inclusions). In 3D polycrystalline materials, crack morphologies can exhibit significant tortuosity due to the inherent heterogeneity within and across grains. Straightforward extension of existing approaches to tortuous cracks in 3D leads to a reduced order basis that may be more costly to prepare and solve even when compared to the full-field models. For instance, each local perturbance (e.g., kink) on a flat crack surface requires an additional basis function to be included in the approach proposed in Ref. [65].

In this manuscript, we propose a new reduced order model that inherits and combines traits of the EHM and POD methodologies. When considered separately, the effectiveness of EHM is limited by the need for extensive crack face partitioning along the crack to accurately capture the behavior in the presence of complex crack surfaces. Mode-decomposition techniques such as POD can address this issue, but they have the disadvantages of being com-

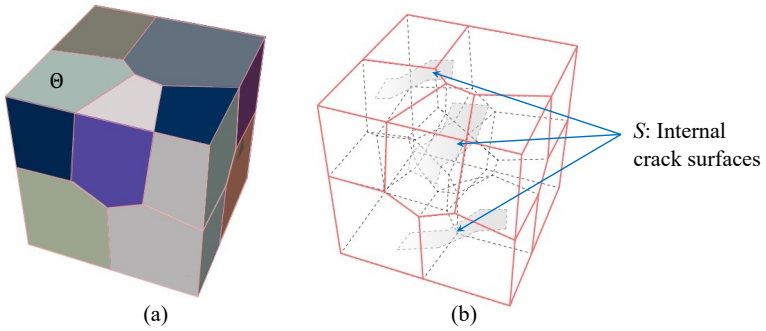

Figure 1. Three-dimensional microstructure with cracks: (a) Polycrystalline volume; and (b) Wire-framed demonstration of the microstructure to show the internal cracks surfaces

putationally expensive to train and highly dependent on the load orientations used in training. By integrating EHM and POD together, the present method allows for the benefits of both EHM's light training stage, and POD's ability to efficiently capture the separation field of complex crack morphologies with small number of basis functions. This manuscript focuses on the reduced order representation of a polycrystalline microstructure with MSC, but does not investigate crack propagation. In addition, while the focus of this manuscript is on MSCs, it's worth noting that the current framework is also applicable to long cracks e.g., in a large polycrystalline microstructure. However, for long cracks, the influence of local texture and crack tip plasticity is negligible, making the classical linear elastic fracture mechanics (LEFM) sufficiently accurate. This framework also accommodates the presence of multiple cracks and takes into account their interactions. The proposed formulation offers three major novelties: (i) the EHM is reformulated with POD to effectively model microstructures with tortuous 3D short cracks; (ii) a constrained optimization problem is developed to solve for the separation coefficients through a combination of reduced order objective function and constraints, avoiding the issue of expressing the contact conditions in the latent space; and (iii) an integrated form of the contact constraints is devised, enabling the use of only one constraint equation regardless of the complexity of the crack morphology.

The remainder of the manuscript is organized as follows: The EHM is reformulated with POD to form the reduced order problem in Section 2. The constrained optimization problem to solve for the separation field coefficients and the integrated form of constraints are discussed in Section 3. The construction of the separation basis function and a brief introduction to POD algorithm are provided in Section 4. Sections 5 discusses the implementation strategy. Section 6 provides numerical verification against direct numerical simulations (DNS) performed using CPFE. Conclusions and future work directions are discussed in Section 7.

2. EHM overview

The EHM formulation, as outlined in [59], is reformulated to incorporate POD into its reduced order kernel for the purpose of modeling short tortuous cracks in 3D polycrystalline volumes. In what follows, we provide an overview of the EHM and discuss the role of POD in its formulation.

As illustrated in Fig. 1, we consider a three dimensional polycrystalline volume $\Theta \subset \mathbb{R}^3$, which contains n_{grain} grains (domain of grain i is denoted as Θ_i; $i = 1, ..., n_{\text{grain}}$) and n_{crack} cracks (domain of crack i is denoted as S_i; $i = 1, ..., n_{\text{crack}}$). We begin with the following ansatz for the strain field:

$$\epsilon_{ij}(\mathbf{y}, t) = A_{ijkl}(\mathbf{y})\bar{\epsilon}_{kl}(t) + \int_{\Theta} g^{\text{ph}}_{ijkl}(\mathbf{y}, \hat{\mathbf{y}})\mu_{kl}(\hat{\mathbf{y}}, t)d\hat{\mathbf{y}} + \int_{S} g^{\text{sep}}_{ijk}(\mathbf{y}, \hat{\mathbf{y}})\delta_k(\hat{\mathbf{y}}, t)d\hat{\mathbf{y}} \tag{1}$$

where $\boldsymbol{\epsilon}$ is the total strain, $\bar{\boldsymbol{\epsilon}}$ is the macroscopic strain that is the volume average of $\boldsymbol{\epsilon}$, $\boldsymbol{\mu}$ is the inelastic strain, and $\boldsymbol{\delta}$ is the separation (or displacement jump) along the crack surfaces ($\mathbf{y} \in S$; $S := \bigcup_{i=1}^{n_{\text{cracks}}} S_i$). $\mathbf{G}$, $\mathbf{g}^{\text{ph}}$ and $\mathbf{g}^{\text{sep}}$ are the polarization functions that are the symmetric gradients of the influence functions $\mathbf{H}$ (the elastic influence function), $\mathbf{h}^{\text{ph}}$ (the inelastic or phase influence function), and $\mathbf{h}^{\text{sep}}$ (the separation influence function), respectively. $\mathbf{A} = \mathbf{G} + \mathbf{I}$ and $\mathbf{I}$ is the fourth order identity tensor.

Substituting Eq. (1) into the equilibrium equation, i.e., $\nabla \cdot \{\mathbf{L}(\mathbf{y}) : [\boldsymbol{\epsilon}(\mathbf{y},t) - \boldsymbol{\mu}(\mathbf{y},t)]\} = 0$ with $\mathbf{L}(\mathbf{y})$ being the elastic moduli, the following alternative form of equilibrium is obtained:

$$\left\{ L_{ijkl}(\mathbf{y}) \left[A_{klmn}(\mathbf{y}) \bar{\epsilon}_{mn}(t) + \int_{\Theta} \left(g^{\text{ph}}_{klmn}(\mathbf{y},\hat{\mathbf{y}}) - I_{klmn}\delta(\mathbf{y}-\hat{\mathbf{y}}) \right) \right. \right. \\ \left. \left. \mu_{mn}(\hat{\mathbf{y}},t) d\hat{\mathbf{y}} + \int_S g^{\text{sep}}_{klm}(\mathbf{y},\hat{\mathbf{y}}) \delta_m(\hat{\mathbf{y}},t) d\hat{\mathbf{y}} \right] \right\}_{,y_j} = 0 \tag{2}$$

where δ is the Dirac delta distribution. Premultiplying Eq. (2) with the separation influence function, integrating by parts over the microstructure domain, and utilizing periodicity yield:

$$t_p(\hat{\mathbf{y}},t) + \int_{\Theta} \left\{ g^{\text{sep}}_{ijp}(\mathbf{y},\hat{\mathbf{y}}) L_{ijkl}(\mathbf{y}) \left[A_{klmn}(\mathbf{y}) \bar{\epsilon}_{mn}(t) + \right. \right. \\ \left. \left. \int_{\Theta} \left(g^{\text{ph}}_{klmn}(\mathbf{y},\tilde{\mathbf{y}}) - I_{klmn}\delta(\mathbf{y}-\tilde{\mathbf{y}}) \right) \mu_{mn}(\tilde{\mathbf{y}},t) d\tilde{\mathbf{y}} + \int_S g^{\text{sep}}_{klm}(\mathbf{y},\tilde{\mathbf{y}}) \delta_m(\tilde{\mathbf{y}},t) d\tilde{\mathbf{y}} \right] \right\} d\mathbf{y} = 0 \tag{3}$$

where $\mathbf{t}$ represents the traction along the crack surface. Equations (2) and (3) are statements of equilibrium defined over the entire microstructure and crack surfaces, respectively. In order to complete the system, Eqs. (2) and (3) are complemented by the evolution equations for the inelastic strain $\boldsymbol{\mu}$ and the contact conditions along the crack surfaces. Inelastic strain exists since the crack fronts or the entire microstructure may deform plastically under the action of applied loading. In the context of crystal plasticity, the evolution of the inelastic strain is described by considering the crystallographic slip along preferred slip orientations i.e., $\dot{\boldsymbol{\mu}} = \sum_{s=1}^{N} \dot{\gamma}^s \mathbf{Z}^s$ with $\dot{\gamma}^s$ being the plastic shearing rate on the s^{th} slip system, N the total number of slip systems, and $\mathbf{Z}^s$ the Schmid tensor uniquely describing the orientation of the s^{th} slip system. Along the crack surfaces, impenetrability is enforced via the unilateral contact conditions:

$$\delta_N(\mathbf{y},t) \geq 0; \quad t_N(\mathbf{y},t) \leq 0; \quad t_N(\mathbf{y},t)\delta_N(\mathbf{y},t) = 0 \tag{4}$$

For simplicity, the crack surfaces are idealized as frictionless:

$$t_{T1}(\mathbf{y},t) = 0; \quad t_{T2}(\mathbf{y},t) = 0 \tag{5}$$

where the subscripts N, $T1$, $T2$ represent the normal, and two tangential components, respectively, of traction and separation.

The EHM formulation proceeds with a reduced order approximation to the inelastic strain and stress fields, following the approach used in [56, 59]:

$$\mu_{ij}(\mathbf{y},t) = \sum_{\alpha=1}^{n} N^{(\alpha)}_{\text{ph}}(\mathbf{y}) \mu^{(\alpha)}_{ij}(t); \qquad \mathbf{y} \in \Theta \tag{6a}$$

$$\sigma_{ij}(\mathbf{y},t) = \sum_{\alpha=1}^{n} N^{(\alpha)}_{\text{ph}}(\mathbf{y}) \sigma^{(\alpha)}_{ij}(t); \qquad \mathbf{y} \in \Theta \tag{6b}$$

where $N^{(\alpha)}_{\text{ph}}$ is the inelastic shape functions, n is the number of reduced order parts within the polycrystal domain, and $\boldsymbol{\sigma}$ is the Cauchy stress ($\boldsymbol{\sigma} = \mathbf{L} : [\boldsymbol{\epsilon} - \boldsymbol{\mu}]$). The choice of the shape function $N^{(\alpha)}_{\text{ph}}$ determines the resulting reduced order system of equations. In this work, we adopt piece-wise constant shape functions as described in [59] to obtain the reduced order system i.e., $N^{(\alpha)}_{\text{ph}} = 1$ if $\mathbf{y} \in \Theta^{(\alpha)}$; $N^{(\alpha)}_{\text{ph}} = 0$ otherwise. $\Theta^{(\alpha)}$ denotes the α^{th} subdomain, i.e., $\Theta = \bigcup_{\alpha=1}^{n} \Theta^{(\alpha)}$ and $\Theta^{(\alpha)} \cap \Theta^{(\beta)} = \emptyset$ for $\alpha \neq \beta$. Therefore, $N^{(\alpha)}_{\text{ph}}$ has local support on $\Theta^{(\alpha)}$. This choice for the reduced order shape functions implies that the reduced order approximation is dependent on the geometry of the microstructure and tied to how and how much the domain Θ is partitioned. In the absence of cracks, the part-per-grain approach where partitioning is based on domains of the grains (i.e., $\Theta^{(\alpha)} = \Theta_i$ for unique $\{\alpha, i\}$ pairs) has been shown to approximate the local and average response field with reasonable accuracy [59]. The presence of cracks in a microstructure poses a challenge for geometry-based domain partitioning scheme used in the reduced order approximation [65]. This is

because the stress and strain concentrations either require extensive partitioning around the crack fronts or lead to higher errors in the response fields. To address this issue, Ref. [65] proposed a strategy that takes both the geometry and the mechanical response into account in order to refine the partitions in the regions around the cracks. This strategy is adopted in the current work.

2.1. Model order reduction for separation field

To complete the model order reduction, we consider the reduced order approximation for the separation field $\boldsymbol{\delta}(\mathbf{y}, t)$. When the crack surface is highly tortuous, extension of the geometry-based model reduction for the separation field may not be feasible. This is because of the restrictions on the continuity of the separation field components. On a flat or a curved crack surface, the separation field components exhibit C^0 continuity. On kinked cracks, discontinuities in the separation components exist, which could be modeled by introducing an additional basis function at each junction point [65]. For rough surfaces in a 3D setting, this strategy results in a very high dimensional basis. Instead, we propose to use a mode based model reduction for the separation field by leveraging POD. Assuming that an appropriate POD basis is available, the reduced order approximation of the separation field is written as:

$$\delta_i(\mathbf{y}, t) = \sum_{\gamma=1}^{n_b} \phi_i^{(\gamma)}(\mathbf{y})\delta^{(\gamma)}(t); \quad \mathbf{y} \in S \tag{7}$$

where $\boldsymbol{\phi}^{(\gamma)}$ is the vector of basis functions obtained from POD, n_b is the number of basis functions, and $\delta^{(\gamma)}$ is the associated coefficient. Another key distinction between Eq. (7) and previous geometry-based representations in [65] is that the separation basis function for each component is different (here the vectorized representation of $\boldsymbol{\phi}^{(\gamma)}$). A scalar coefficient is associated with each basis which leads to the lowest overall computational cost. It is possible to extend the formulation to consider vectorized or tensor coefficients for a given model basis, but this possibility is not explored in this study. The coefficients are expressed in terms of a non-local weighting function as:

$$\delta^{(\gamma)}(t) = \int_s \psi_i^{(\gamma)}(\mathbf{y})\delta_i(\mathbf{y}, t)d\mathbf{y} \tag{8}$$

where $\boldsymbol{\psi}^{(\gamma)}$ is the vector of weighting functions, the components of which are taken to be of the following form:

$$\psi_i^{(\gamma)}(\mathbf{y}) = \xi\phi_i^{(\gamma)}(\mathbf{y}) \tag{9}$$

where ξ is a scalar constant. Substituting Eqs. (7) and (9) into Eq. (8), and considering that the basis functions generated from the POD must be orthonormal to each other i.e., $\int_s \boldsymbol{\phi}^{(\gamma)}(\mathbf{y}) \cdot \boldsymbol{\phi}^{(\eta)}(\mathbf{y})d\mathbf{y} = \delta^{(\gamma\eta)}$ (where $\delta^{(\gamma\eta)}$ is the Kronecker delta), it is then straightforward to conclude that $\xi = 1$ and $\boldsymbol{\psi}^{(\gamma)} = \boldsymbol{\phi}^{(\gamma)}$.

By employing the reduced order approximation for the inelastic strain, stress, and separation fields in Eqs. (6) and (7), and following the procedure outlined in [59], the reduced order version of Eq. (2) is written as:

$$M_{ijkl}^{(\alpha)}\dot{\sigma}_{kl}^{(\alpha)}(t) - \sum_{\beta=1}^{n}(P_{ijkl}^{(\alpha\beta)} - \delta^{(\alpha\beta)}I_{ijkl})\dot{\mu}_{kl}^{(\beta)}(t) - \sum_{\gamma=1}^{n_b} R_{ij}^{(\alpha\gamma)}\dot{\delta}^{(\gamma)}(t) = A_{ijkl}^{(\alpha)}\dot{\bar{\epsilon}}_{kl}(t) \tag{10}$$

where,

$$\mu_{ij}^{(\alpha)}(t) = \int_\Theta \psi_{\text{ph}}^{(\alpha)}(\mathbf{y})\mu_{ij}(\mathbf{y}, t)d\mathbf{y} \tag{11a}$$

$$M_{ijkl}^{(\alpha)} = \int_\Theta \psi_{\text{ph}}^{(\alpha)}(\mathbf{y})M_{ijkl}(\mathbf{y})N_{\text{ph}}^{(\alpha)}(\mathbf{y})d\mathbf{y} \tag{11b}$$

$$P_{ijkl}^{(\alpha\beta)} = \int_\Theta \psi_{\text{ph}}^{(\alpha)}(\mathbf{y})h_{(i,j)kl}^{\text{ph},(\beta)}(\mathbf{y})d\mathbf{y} \tag{11c}$$

$$A_{ijkl}^{(\alpha)} = \int_\Theta \psi_{\text{ph}}^{(\alpha)}(\mathbf{y})A_{ijkl}(\mathbf{y})d\mathbf{y} \tag{11d}$$

$$R_{ij}^{(\alpha\gamma)} = \int_{\Theta} \psi_{\text{ph}}^{(\alpha)}(\mathbf{y}) h_{(i,y_j)}^{\text{sep},(\gamma)}(\mathbf{y}) d(\mathbf{y}) \tag{11e}$$

in which $\mathbf{M} = \mathbf{L}^{-1}$ is the compliance tensor. Similarly, the reduced order version of Eq. (3) is expressed as:

$$t^{(\gamma)}(t) + C_{mn}^{(\gamma)} \bar{\epsilon}_{mn}(t) + \sum_{\eta=1}^{n_b} D^{(\gamma\eta)} \delta^{(\eta)}(t) + \sum_{\beta=1}^{n} T_{mn}^{(\gamma\beta)} \mu_{mn}^{(\beta)}(t) = 0 \tag{12}$$

where

$$t^{(\gamma)}(t) = \int_S \psi_i^{(\gamma)}(\mathbf{y}) t_i(\mathbf{y}, t) d\mathbf{y} \tag{13a}$$

$$C_{mn}^{(\gamma)} = \int_{\Theta} h_{(i,y_j)}^{\text{sep},(\gamma)}(\mathbf{y}) L_{ijkl}(\mathbf{y}) A_{klmn}(\mathbf{y}) d\mathbf{y} \tag{13b}$$

$$D^{(\gamma\eta)} = \int_{\Theta} h_{(i,y_j)}^{\text{sep},(\gamma)}(\mathbf{y}) L_{ijkl}(\mathbf{y}) h_{(k,y_l)}^{\text{sep},(\gamma)}(\mathbf{y}) d\mathbf{y} \tag{13c}$$

$$T_{mn}^{(\gamma\alpha)} = \int_{\Theta} h_{(i,y_j)}^{\text{sep},(\gamma)}(\mathbf{y}) L_{ijkl}(\mathbf{y}) S_{klmn}^{(\alpha)}(\mathbf{y}) d\mathbf{y} \tag{13d}$$

in which $\mathbf{h}^{\text{ph},(\alpha)}$ and $\mathbf{h}^{\text{sep},(\gamma)}$ are the integrated influence functions:

$$h_{ikl}^{\text{ph},(\alpha)}(\mathbf{y}) := \int_{\Theta} N_{ph}^{(\alpha)}(\hat{\mathbf{y}}) h_{ikl}^{\text{ph}}(\mathbf{y}, \hat{\mathbf{y}}) d\hat{\mathbf{y}} \tag{14}$$

$$h_i^{\text{sep},(\gamma)}(\mathbf{y}) := \int_S \phi_p^{(\gamma)}(\hat{\mathbf{y}}) h_{ip}^{\text{sep}}(\mathbf{y}, \hat{\mathbf{y}}) d\hat{\mathbf{y}} \tag{15}$$

The reduced order system can be viewed as a system of three sets of coupled non-linear equations i.e., (i) Eq. (10), (ii) Eq. (12) along with the crack surface contact interaction conditions in Eqs. (4) and (5), and (iii) the evolution equations for $\boldsymbol{\mu}^{(\alpha)}$ (see e.g., [60, 66]). The stress coefficients $\boldsymbol{\sigma}^{(\alpha)}$, the separation coefficients $\delta^{(\gamma)}$, and the inelastic strain coefficients $\boldsymbol{\mu}^{(\alpha)}$ are the primary unknowns.

The current formulation leverages the framework of EHM, and POD is only applied to identify the basis functions for the separation field $\boldsymbol{\delta}$. For all other constitutive-related variables, including stress and inelastic strain, model order reduction using piece-wise constant shape functions is employed. The use of piece-wise constant shape functions facilitates the recovery of constitutive relations in the reduced space, as only part-averaged quantities need to be tracked. This mixed approach ensures that the model can be generalized to a wide range of material behaviors while simultaneously allowing for the accommodation of tortuous crack surfaces.

3. The constrained optimization problem

A tightly coupled Newton-Raphson (N-R) method [67] or a multi-level staggered scheme [68] could be used to solve the reduced order system of equations derived in Section 2.1. In the current work, the latter is adopted, in which the three sets of reduced order equations are solved in a coupled but staggered manner [65]. In this work, we focus on the evaluation of Eq. (12) with the contact behavior.

The incremental procedure for evaluating the separation coefficients $\delta^{(\gamma)}$ as part of the staggered scheme is summarized in Box I. It is important to note that the unilateral contact conditions need to be imposed throughout the crack surface (i.e., $\forall \mathbf{y} \in \mathbf{S}$). While the alternative equation collocated on the crack surface (Eq. (12)) is expressed in terms of the field coefficients alone (i.e., $\delta^{(\gamma)}$, $\boldsymbol{\mu}^{(\gamma)}$ and no $\mathbf{y}$ dependence), expressing the contact condition using the field coefficients alone does not appear to be obvious and straightforward. Refs. [63, 65] proposed a set of strictly non-negative separation basis functions. In this case, impenetrability constraint could be enforced by restricting the field coefficients to be non-negative as well. This approach is not possible when the separation basis is constructed using POD. Even when the snapshots used to generate the reduced basis uniformly satisfy contact constraints, the basis functions themselves do not necessarily satisfy them. This has been demonstrated in Ref. [69], where snapshots that

are all positive everywhere results in POD basis with basis functions that are not positive everywhere. In Ref. [69], an approach to ensure non-negativity of the basis functions is also proposed, but at the price of sacrificing orthonormality. Consequently, this particular approach is unsuitable for the current purpose as the reduced order equations require orthonormality. In this section, we reformulate SF1 in Box I where the contact constraints can be imposed in an efficient fashion.

Given the coefficient tensors, $\mathbf{C}^{(\gamma)}$, $\mathbf{D}^{(\gamma\eta)}$ and $\mathbf{T}^{(\gamma\beta)}$, the macroscopic strain $\bar{\boldsymbol{\epsilon}}$ at time ${}_{l+1}t$, the inelastic strain coefficients $\boldsymbol{\mu}^{(\alpha)}$ at time ${}_{l}t$. *Find* the separation coefficients $\boldsymbol{\delta}^{(\gamma)}$ at time ${}_{l+1}t$ such that:

- Equilibrium ($\gamma = 1, 2, \ldots, n_{\mathrm{b}}$):

$$t^{(\gamma)}({}_{l+1}t) + C^{(\gamma)}_{mn}\bar{\epsilon}_{mn}({}_{l+1}t) + \sum_{\eta=1}^{n_b} D^{(\gamma\eta)}\delta^{(\eta)}({}_{l+1}t) + \sum_{\beta=1}^{n} T^{(\gamma\beta)}_{mn}\mu^{(\beta)}_{mn}({}_{l}t) = 0;$$

- Subjected to unilateral contact conditions:

$$\delta_N(\mathbf{y}, {}_{l+1}t) \geq 0; \quad t_N(\mathbf{y}, {}_{l+1}t) \leq 0; \quad \delta_N(\mathbf{y}, {}_{l+1}t)t_N(\mathbf{y}, {}_{l+1}t) = 0; \quad \forall \mathbf{y} \in \mathbf{S}$$

. Box I: Problem SF1: Reduced order equation for solving Eq. (12)

Given the coefficient tensors, $\mathbf{C}^{(\gamma)}$, $\mathbf{D}^{(\gamma\eta)}$ and $\mathbf{T}^{(\gamma\beta)}$, the macroscopic strain $\bar{\boldsymbol{\epsilon}}$ at time ${}_{l+1}t$, the inelastic strain coefficients $\boldsymbol{\mu}^{(\alpha)}$ at time ${}_{l}t$. *Find* the separation coefficients $\boldsymbol{\delta}^{(\gamma)}$ at time ${}_{l+1}t$ such that:

- The objective function:

$$\sum_{\gamma=1}^{n_b}\left\{\frac{1}{2}\delta^{(\gamma)}({}_{l+1}t)\sum_{\eta=1}^{n_b} D^{(\gamma\eta)}\delta^{(\eta)}({}_{l+1}t) + \delta^{(\gamma)}({}_{l+1}t)\left[C^{(\gamma)}_{mn}\bar{\epsilon}_{mn}({}_{l+1}t) + \sum_{\beta=1}^{n} T^{(\gamma\beta)}_{mn}\mu^{(\beta)}_{mn}({}_{l}t)\right]\right\}$$

- is minimized under the constraint:

$$\delta_N(\mathbf{y}, {}_{l+1}t) \geq 0$$

. Box II: Problem SF2: The constrained optimization problem

The constrained root-finding problem (SF1) described in Box I could be posed as a constrained optimization problem (SF2) defined in Box II. In the following, we demonstrate that the solution to Problem SF2 (Box II) is also the solution to the Problem SF1. Since the constraint function $\delta_N(\mathbf{y},{}_{l+1}\,t) \geq 0$ is a function of the continuous field $\mathbf{y}$, SF2 can be considered as a semi-infinite programming (SIP) problem [70]. Integrating the constraint in Box II with a non-negative function $\tilde{\lambda}(\mathbf{y})$ over the crack domain:

$$\int_S \tilde{\lambda}(\mathbf{y})\delta_N(\mathbf{y}, {}_{l+1}t)d\mathbf{y} \geq 0 \tag{16}$$

Considering the alternative (weak) constraint above (Eq. (16)), we define an auxiliary problem (Problem SF3) shown in Box III. The optimization problem in Box III is not equivalent to Box II since the strong constraint ($\delta_N(\mathbf{y},{}_{l+1}\,t) \geq 0$) implies the weak constraint, but the weak constraint does not imply the strong constraint. Let ψ^{II} and ψ^{III} denote the space of feasible solutions (i.e., solutions that satisfy the inequality constraints) for SF2 and SF3, respectively. Naturally, ψ^{II} is a subset of ψ^{III} (i.e., $\psi^{II} \subset \psi^{III}$).

SF3 is a standard nonlinear programming problem with $\delta^{(\gamma)}$ as the discrete set of unknowns. Denoting $\Delta^* = \left\{\delta^{*(1)}, ..., \delta^{*(n_b)}\right\}$ as a local minima and using Eq. (7), SF3 is expressed using the Karush-Kuhn-Tucker (KKT) conditions

Given the coefficient tensors, $\mathbf{C}^{(\gamma)}$, $\mathbf{D}^{(\gamma\eta)}$ and $\mathbf{T}^{(\gamma\beta)}$, the macroscopic strain $\bar{\boldsymbol{\epsilon}}$ at time ${}_{l+1}t$, the inelastic strain coefficients $\boldsymbol{\mu}^{(\alpha)}$ at time ${}_{l}t$. *Find* the separation coefficients $\boldsymbol{\delta}^{(\gamma)}$ at time ${}_{l+1}t$ such that:

- The objective function:

$$f(\Delta, {}_{l+1}t) = \sum_{\gamma=1}^{n_b} \left\{ \frac{1}{2} \sum_{\eta=1}^{n_b} \delta^{(\gamma)}({}_{l+1}t) D^{(\gamma\eta)} \delta^{(\eta)}({}_{l+1}t) + \delta^{(\gamma)}({}_{l+1}t) \left[C^{(\gamma)}_{mn} \bar{\epsilon}_{mn}({}_{l+1}t) + \sum_{\beta=1}^{n} T^{(\gamma\beta)}_{mn} \mu^{(\beta)}_{mn}({}_{l}t) \right] \right\}$$

- is minimized under the constraint:

$$g(\Delta, {}_{l+1}t) = -\int_S \tilde{\lambda}(\mathbf{y}) \delta_N(\mathbf{y}, {}_{l+1}t) d\mathbf{y} = -\sum_{\gamma=1}^{n_b} \delta^{(\gamma)}({}_{l+1}t) \int_S \tilde{\lambda}(\mathbf{y}) \phi_N^{(\gamma)}(\mathbf{y}) d\mathbf{y} \leq 0$$

where $\Delta = \left\{ \delta^{(1)}, ..., \delta^{(n_b)} \right\} \in (R^+)^{n_b}$.

. Box III: SF3: The constrained optimization problem with weak constraint

(using Eq. (7)):

- Stationary:

$$\frac{\partial f}{\partial \delta^{(\gamma)}}(\Delta^*, {}_{l+1}t) + \frac{\partial g}{\partial \delta^{(\gamma)}}(\Delta^*, {}_{l+1}t) = C^{(\gamma)}_{mn} \bar{\epsilon}_{mn}({}_{l+1}t) + \sum_{\eta=1}^{n_b} D^{(\gamma\eta)} \delta^{*(\eta)}({}_{l+1}t) + \sum_{\beta=1}^{n} T^{(\gamma\beta)}_{mn} \mu^{(\beta)}_{mn}({}_{l}t) - \hat{t}^{(\gamma)}({}_{l+1}t) \tag{17}$$

- KKT conditions:

$$g(\Delta^*, {}_{l+1}t) \leq 0; \quad \hat{\lambda}({}_{l+1}t) \geq 0; \quad \hat{\lambda}({}_{l+1}t) g(\Delta^*, {}_{l+1}t) = 0 \tag{18}$$

where

$$\hat{t}^{(\gamma)}({}_{l+1}t) = -\int_S \lambda(\mathbf{y}, {}_{l+1}t) \phi_N^{(\gamma)}(\mathbf{y}) d\mathbf{y} \tag{19}$$

in which,

$$\lambda(\mathbf{y}, {}_{l+1}t) = \hat{\lambda}({}_{l+1}t) \tilde{\lambda}(\mathbf{y}) \geq 0 \tag{20}$$

and $\hat{\lambda}$ is a Lagrange multiplier. Considering the definition of $t^{(\gamma)}$ in Eq. (13a), and utilizing Eqs. (5) and (9) yield:

$$t^{(\gamma)}({}_{l+1}t) = \int_S \phi_N^{(\gamma)}(\mathbf{y}) t_N(\mathbf{y}, {}_{l+1}t) d\mathbf{y} \tag{21}$$

Comparing Eq. (21) with Eq. (19), we observe that $\hat{t}^{(\gamma)} = t^{(\gamma)}$ if

$$t_N(\mathbf{y}, {}_{l+1}t) = -\lambda(\mathbf{y}, {}_{l+1}t) \leq 0 \tag{22}$$

Consider the complementary slackness in KKT conditions:

$$\hat{\lambda}({}_{l+1}t) g(\Delta^*, {}_{l+1}t) = \hat{\lambda}({}_{l+1}t) \int_S \tilde{\lambda}(\mathbf{y}) \delta_N^*(\mathbf{y}) d\mathbf{y} = \int_S \lambda(\mathbf{y}, {}_{l+1}t) \delta_N^*(\mathbf{y}) d\mathbf{y} = 0 \tag{23}$$

where $\delta_N^*(\mathbf{y}, {}_{l+1}t) = \sum_{\gamma=1}^{n_b} \delta^{*(\gamma)}({}_{l+1}t) \phi_N^{(\gamma)}(\mathbf{y})$. Substituting Eq. (22) into Eq. (23) yields:

$$\int_S t_N(\mathbf{y}, {}_{l+1}t) \delta_N^*(\mathbf{y}, {}_{l+1}t) d\mathbf{y} = 0 \tag{24}$$

By choosing $\tilde{\lambda}$ such that Eq. (22) is satisfied, SF3 is rewritten as:

$$t^{(\gamma)} + C^{(\gamma)}_{mn}\bar{\epsilon}_{mn} + \sum_{\eta=1}^{n_b} D^{(\gamma\eta)}\delta^{*(\eta)} + \sum_{\beta=1}^{n} T^{(\gamma\beta)}_{mn}\mu^{(\beta)}_{mn} = 0 \tag{25}$$

subjected to $\delta^*_N \geq 0$, and the constraints in Eq. (22) and Eq. (24). This form is similar to SF1, but with the weak condition provided in Eq. (24).

Let $\Delta^{\triangle} \in \psi^{II}$ is a solution to SF2. Since $\psi^{II} \subset \psi^{III}$, $\Delta^{\triangle}$ satisfy Eqs. (22) and (24) as well. Noting that Δ^{Δ} also satisfies the impenetrability condition by definition i.e., $\delta^{\triangle}_N(\mathbf{y},\, {}_{l+1}t) = \sum_{\gamma=1}^{n_b} \delta^{\triangle(\gamma)}({}_{l+1}t)\phi^{(\gamma)}_N(\mathbf{y}) \geq 0$, and that the normal traction is non-positive: $t_N(\mathbf{y},\, {}_{l+1}t)\delta^{\triangle}_N(\mathbf{y},\, {}_{l+1}t) \leq 0$ (by Eq. (22)). Together with the weak constraint (Eq. (24)), we conclude:

$$t_N(\mathbf{y},\, {}_{l+1}t)\delta^{\triangle}_N(\mathbf{y},\, {}_{l+1}t) = 0 \tag{26}$$

as the integral of a non-positive function is zero only when the function itself is zero. Combining Eqs. (22), (25), (26), and the constraint in SF2, it can be concluded that the solution to SF2 also satisfies the equilibrium equation and the unilateral contact conditions shown in Box I.

In order to address the aforementioned challenges associated with the direct implementation of the separation constraint in SF2, we utilize an integrated form of the constraint that removes the dependence on the spatial coordinate $\mathbf{y}$. Consider the following form:

$$\int_S \{|\delta_N(\mathbf{y},\, {}_{l+1}t)| - \delta_N(\mathbf{y},\, {}_{l+1}t)\}\, d\mathbf{y} = 0 \tag{27}$$

It is straightforward to show that:

$$\int_S \{|\delta_N(\mathbf{y},\, {}_{l+1}t)| - \delta_N(\mathbf{y},\, {}_{l+1}t)\}\, d\mathbf{y} = 0 \Longleftrightarrow \delta_N(\mathbf{y},\, {}_{l+1}t) \geq 0 \tag{28}$$

The benefit of the integrated form of the proposed constraint (Eq. (27)) is that it is independent of $\mathbf{y}$. This means that regardless of the complexity of the crack morphology, a single impenetrability constraint equation (that is a function of all separation coefficients) can be used. The reformulated constrained optimization problem with the integrated constraints is summarized as problem SF4 in Box IV.

Given the coefficient tensors, $\mathbf{C}^{(\gamma)}$, $\mathbf{D}^{(\gamma\eta)}$ and $\mathbf{T}^{(\gamma\beta)}$, the macroscopic strain $\bar{\boldsymbol{\epsilon}}$ at time ${}_{l+1}t$, the inelastic strain coefficients $\boldsymbol{\mu}^{(\alpha)}$ at time ${}_{l}t$. *Find* the separation coefficients $\boldsymbol{\delta}^{(\gamma)}$ at time ${}_{l+1}t$ such that:

- The objective function:

$$f(\Delta_{,l+1}\, t) = \sum_{\gamma=1}^{n_b}\left\{\frac{1}{2}\sum_{\eta=1}^{n_b}\delta^{(\gamma)}({}_{l+1}t)D^{(\gamma\eta)}\delta^{(\eta)}({}_{l+1}t) + \delta^{(\gamma)}({}_{l+1}t)\left[C^{(\gamma)}_{mn}\bar{\epsilon}_{mn}({}_{l+1}t) + \sum_{\beta=1}^{n} T^{(\gamma\beta)}_{mn}\mu^{(\beta)}_{mn}({}_{l}t)\right]\right\}$$

- is minimized under the constraint:

$$\int_S \{|\delta_N(\mathbf{y},\, {}_{l+1}t)| - \delta_N(\mathbf{y},\, {}_{l+1}t)\}\, d\mathbf{y} = 0$$

. Box IV: SF4: The constrained optimization problem with integrated constraints

4. Separation basis function construction with POD

Standard application of POD to represent microstructure behavior relies on generating a suite of snapshots by performing a series of nonlinear microstructural analyses [71, 72]. Leveraging the structure of EHM and homogenization

process, the current study generates snapshots from a much simpler analysis. Let $\bar{\boldsymbol{\epsilon}}^*$ denote a macroscopic strain state. We consider the following microstructure problem to generate the snapshots:

$$\left\{L_{ijkl}(\mathbf{y})u_{(k,y_l)}(\mathbf{y})\right\}_{,y_j} = -\left\{L_{ijkl}(\mathbf{y})\epsilon^*_{kl}\right\}_{,y_j}; \qquad \mathbf{y} \in \Theta \tag{29}$$

in which $\mathbf{u}$ is the response field. Periodicity is applied along the microstructure domain boundaries $\partial\Theta$, and impenetrability condition is considered on the crack surface S:

$$[\![u_i(\mathbf{y})]\!]n_i(\mathbf{y}) \geq 0; \quad \mathbf{y} \in S \tag{30}$$

where $[\![\cdot]\!]$ is the jump operator i.e., $[\![\mathbf{u}(\mathbf{y})]\!] = \mathbf{u}|_{S_-} - \mathbf{u}|_{S_+}$, and $\mathbf{n}$ is the associated normal direction. Given that Eq. (29) does not include material nonlinearity, we are interested in sampling load orientations. Hence, the macroscopic load state is considered normalized i.e., $\|\bar{\boldsymbol{\epsilon}}^*\|_2 = 1$. A snapshot is then obtained as $\boldsymbol{\delta}^* = [\![\mathbf{u}(\mathbf{y})]\!]$ subjected to $\bar{\boldsymbol{\epsilon}}^*$. In order to build the POD basis, n_{snp} snapshots are generated by sampling the normalized macroscopic strain space. Naturally, the resultant POD basis as well as the accuracy of the reduced order model are influenced by the number and directions of the loadings. The strategy of selecting the external loading is discussed with more details in Section 5.

The procedure of performing POD can be found in a wide range of literature sources. For a more comprehensive and rigorous discussion of POD and its application in solid mechanics, we refer to Refs. [71, 73–75]. In this section, we discuss the POD algorithm to specifically identify the separation basis functions $\boldsymbol{\phi}^{(\gamma)}$. Given the ensemble of snapshots $\mathbf{X} = \left\{\boldsymbol{\delta}^1(\mathbf{y}), ..., \boldsymbol{\delta}^{n_{\text{snp}}}(\mathbf{y})\right\}$, find a set of orthonormal basis functions $\boldsymbol{\Phi} = \left\{\boldsymbol{\phi}^1(\mathbf{y}), ..., \boldsymbol{\phi}^{n_b}(\mathbf{y})\right\}$ such that the error defined as:

$$e(n_\phi) := \sum_{k=1}^{n_{\text{snp}}} \|\boldsymbol{\delta}^k(\mathbf{y}) - \tilde{\boldsymbol{\delta}}^k(\mathbf{y})\|_2^2 \tag{31}$$

is minimized, where n_{snp} is the number of snapshots, $\tilde{\boldsymbol{\delta}}^k$ represents the projection of $\boldsymbol{\delta}^k$ on to the subspace spanned by the basis functions $\boldsymbol{\Phi}$, i.e., $\tilde{\boldsymbol{\delta}}^k = \sum_{i=1}^{n_b} \boldsymbol{\phi}^i(\boldsymbol{\phi}^i \cdot \boldsymbol{\delta}^k)$, and $\|\cdot\|_2$ denotes the L2 norm.

For a finite element discretization of the crack surface, $\boldsymbol{\delta}^k(\mathbf{y})$ and $\tilde{\boldsymbol{\delta}}^k(\mathbf{y})$ are written in matrix representation as:

$$\boldsymbol{\delta}^k(\mathbf{y}) = [\mathcal{N}(\mathbf{y})]\left[X^k\right] \tag{32}$$

$$\tilde{\boldsymbol{\delta}}^k(\mathbf{y}) = [\mathcal{N}(\mathbf{y})]\left[\tilde{X}^k\right] \tag{33}$$

respectively, where $\left[X^k\right]$ and $\left[\tilde{X}^k\right]$ are the vectors that contain the nodal values of the two functions.

$$[\mathcal{N}(\mathbf{y})] = \left[\begin{bmatrix} N_1(\mathbf{y}) & 0 & 0 \\ 0 & N_1(\mathbf{y}) & 0 \\ 0 & 0 & N_1(\mathbf{y}) \end{bmatrix} \quad ... \quad \begin{bmatrix} N_{n_{\text{node}}}(\mathbf{y}) & 0 & 0 \\ 0 & N_{n_{\text{node}}}(\mathbf{y}) & 0 \\ 0 & 0 & N_{n_{\text{node}}}(\mathbf{y}) \end{bmatrix}\right] \tag{34}$$

in which $N_I(\mathbf{y})$ is the shape function associated with I^{th} node, and n_{node} is the number of nodes on the crack surface. Operating on Eq. (31) and substituting with Eqs. (32) and (33) yield:

$$\begin{aligned} &\sum_{k=1}^{n_{\text{snp}}} \|\boldsymbol{\delta}^k(\mathbf{y}) - \tilde{\boldsymbol{\delta}}^k(\mathbf{y})\|_2^2 = \sum_{k=1}^{n_{\text{snp}}} \int_S |\boldsymbol{\delta}^k(\mathbf{y}) - \tilde{\boldsymbol{\delta}}^k(\mathbf{y})|^2 d\mathbf{y} \\ &= \sum_{k=1}^{n_{\text{snp}}} \left\{\left[\bar{M}\right]\left[X^k\right] - \left[\bar{M}\right]\left[\tilde{X}^k\right]\right\}^T \left\{\left[\bar{M}\right]\left[X^k\right] - \left[\bar{M}\right]\left[\tilde{X}^k\right]\right\} \end{aligned} \tag{35}$$

where $[M]$ is the geometric mass matrix:

$$[M] = \int_S [\mathcal{N}(\mathbf{y})]^T [\mathcal{N}(\mathbf{y})]\, d\mathbf{y} \tag{36}$$

and $\left[\bar{M}\right]$ is from the Cholesky decomposition of $[M]$ i.e., $[M] = \left[\bar{M}\right]^T \left[\bar{M}\right]$.

Minimizing Eq. (35) is a standard principal component analysis (PCA) problem, the solution of which can be obtained through singular value decomposition (SVD). The POD algorithm is as follows [75]:

Algorithm 1 SVD-based computation of POD basis for separation fields

Require: Snapshots matrix $[X] \in \mathbb{R}^{3n_{\text{node}} \times n_{\text{snp}}}$, $\left[\bar{M}\right] \in \mathbb{R}^{3n_{\text{node}} \times 3n_{\text{node}}}$
Ensure: The basis function $\mathbf{\Phi}$

1. $\left[\bar{X}\right] = \left[\bar{M}\right][X]$
2. Compute singular value decomposition $\left[\bar{X}\right] = [U][\Sigma][V]^T$
3. Choose dimension of truncated basis $n_b \in \{1, 2, ..., \min(n_{\text{snp}}, \text{rank}(\bar{X})\}$
4. Choose first n_b columns of $[\Phi] = \left(\left[\bar{M}\right]^{-1} [U]\right)[:, 0 : n_b]$
5. Recover the basis function as $\mathbf{\Phi} = [\mathcal{N}][\Phi]$

where $[X]$ is the matrix of the nodal values of all separations in the training data i.e., $[X] = \left[\left[X^1\right], ..., [X^{n_{\text{snp}}}]\right]$.

The number of basis functions, n_b, naturally affects the computational efficiency and accuracy of the reduced order model. It can be shown that as $n_b = \min(n_{\text{snp}}, \text{rank}(\bar{X}))$, the error defined in Eq. (31) is minimized. The number of basis functions needed to provide an accurate approximation is discussed in the numerical verification section.

5. Computational implementation

Figure 2 presents an overview of the overall implementation strategy, which consists of two stages: model training and model execution. In what follows, an overview of each stage is provided, with an emphasis on the discussion of the snapshot generation strategy in the model training stage.

5.1. Model training stage

The model training stage involves the following steps: (i) microstructure construction, (ii) phase partitioning, (iii) snapshots generation, (iv) separation basis construction, and (v) coefficient tensor computation. In the microstructure construction stage, we begin by generating the polycrystal microstructure geometry and the geometry of the cracks. Neper software [76] is employed to create and mesh the polycrystalline microstructure without cracks. GMSH [77] is used to generate and mesh the crack surface with customized crack morphologies. To insert the crack surface mesh into the polycrystalline microstructure, the commercial software Z-cracks is used. Z-cracks employs remeshing techniques to perform the crack insertion [78]. The snapshot generation stage consists of identifying the set of normalized macroscopic strains, and solving the snapshot generation problem stated in Section 4. The strategy is discussed in detail below. The separation basis construction consists of POD performed using the snapshots as described in Section 4. The coefficient tensors are computed on the mesh generated in the microstructure construction step using the phase and separation basis functions. An auto-clustering algorithm as proposed in [65] is employed to refine the reduced order parts near the crack fronts. This algorithm is based on energy measure and automatically refines the regions where stress or strain concentrations occur. The elastic and phase influence functions are computed by evaluating the linear elastic influence function problems described in e.g., [59]. The separation influence functions are solved by enforcing the basis function as the separation fields as described in [65]. The influence functions are then integrated to obtain the coefficient tensors via Eqs. (11b-11e) and (13b-13d)

5.1.1. Snapshot generation strategy

It is well-known that the incorporation of a priori knowledge in the generation of snapshots can greatly improve the accuracy and efficiency of resultant ROM [71, 79, 80]. Specifically, using a priori knowledge to guide the selection of snapshots can reduce the amount of training data required and the number of basis functions needed to accurately represent the system's behavior. In the context of this study, a priori knowledge refers to the knowledge of the loading to be imposed on the microstructure. However, this information is not typically available. For instance, in the case

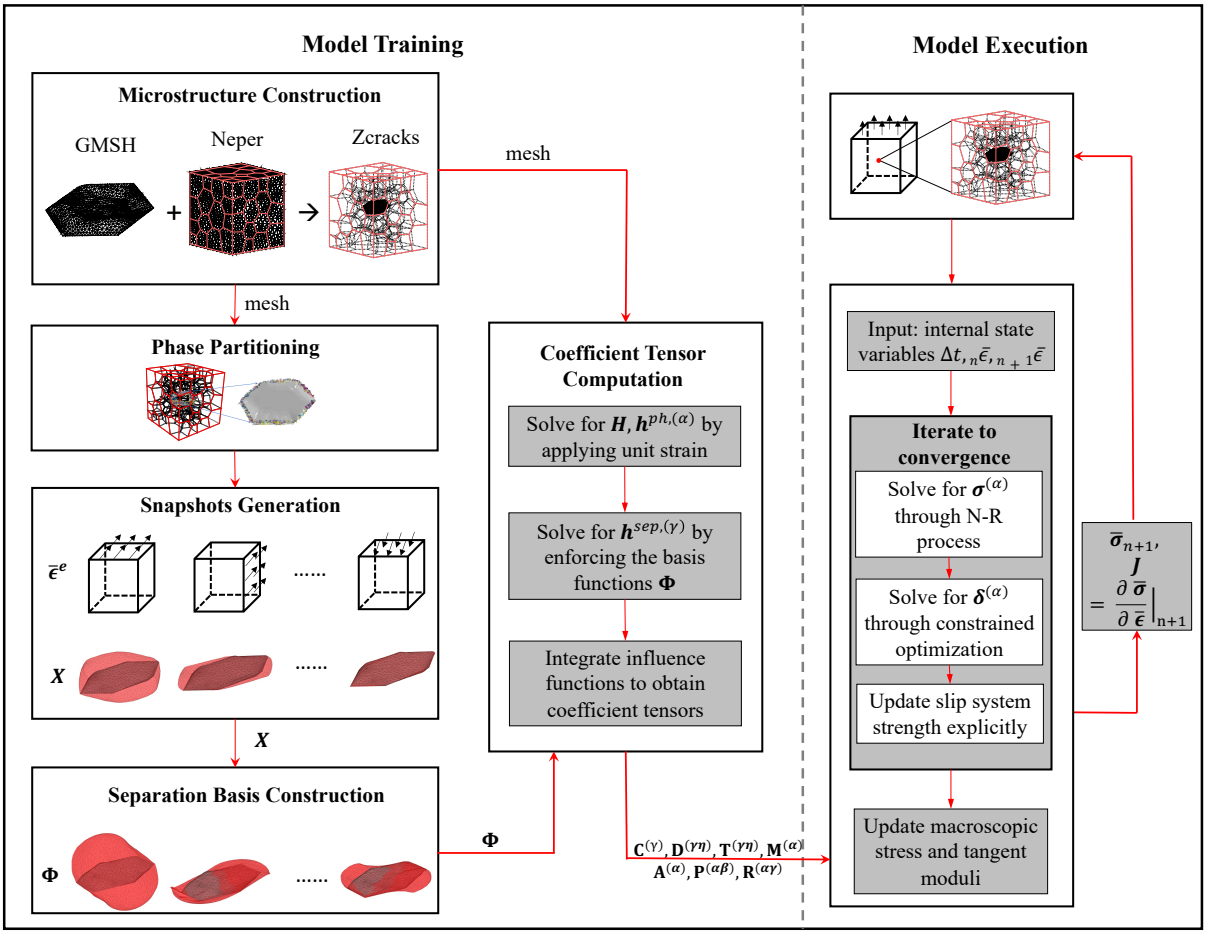

Figure 2. Overview of implementation strategy

when the ROM is used in the context of multiscale modeling (e.g., [60]), different quadrature points of a macroscopic structural domain, represented by the ROM experience different load histories, and the loading conditions for any of the quadrature points are not known in advance. In order to build a model that accurately predicts the separation fields with no implicit knowledge of the loading conditions, it is necessary to use snapshots that span the space of possible loading conditions. One way of achieving this is to evenly sample the space. This process is equivalent to evenly sampling from a 6-dimensional unit sphere because the normalized macroscale strain, $\bar{\boldsymbol{\epsilon}}^*$ is a 6-dimensional unit tensor.

Evenly sampling a high-dimensional unit sphere is equivalent to the Tammes problem in geometry (i.e., packing a given number of points on the surface of a sphere such that the minimum distance between points is maximized) [81] or the generalized Thomson problem in physics (i.e., determining the minimum electrostatic potential energy configuration of n electrons constrained to the surface of a unit sphere that repel each other with a force given) [82]. An exact solution to this problem has not been discovered. Approximate solutions include: (i) simulation-based approaches (e.g., using electron repulsion) [83]; (ii) hypercube rejection [84]; and (iii) spiral approximation (e.g., using the Fibonacci sphere) [85]. A thorough discussion and implementation details of the above methods can be found in [86]. In the current study, we adopt the implementation from [87], which employs a particle simulation-based optimization process that encourages all vectors to be equidistant from their nearest neighbors. An illustration of the results from this implementation is shown in Fig. 3 for 2D, 3D and 6D unit spheres. It is visually evident that the points are evenly distributed in 2D and 3D cases, as shown in Fig. 3(a) and (b). In 6D, the distribution of the distances between

each point and its nearest neighbors is plotted in Fig. 3(c). The concentrated distribution in Fig. 3(c) shows that this distance is approximately the same for all points, which indicates evenly distributed sampling.

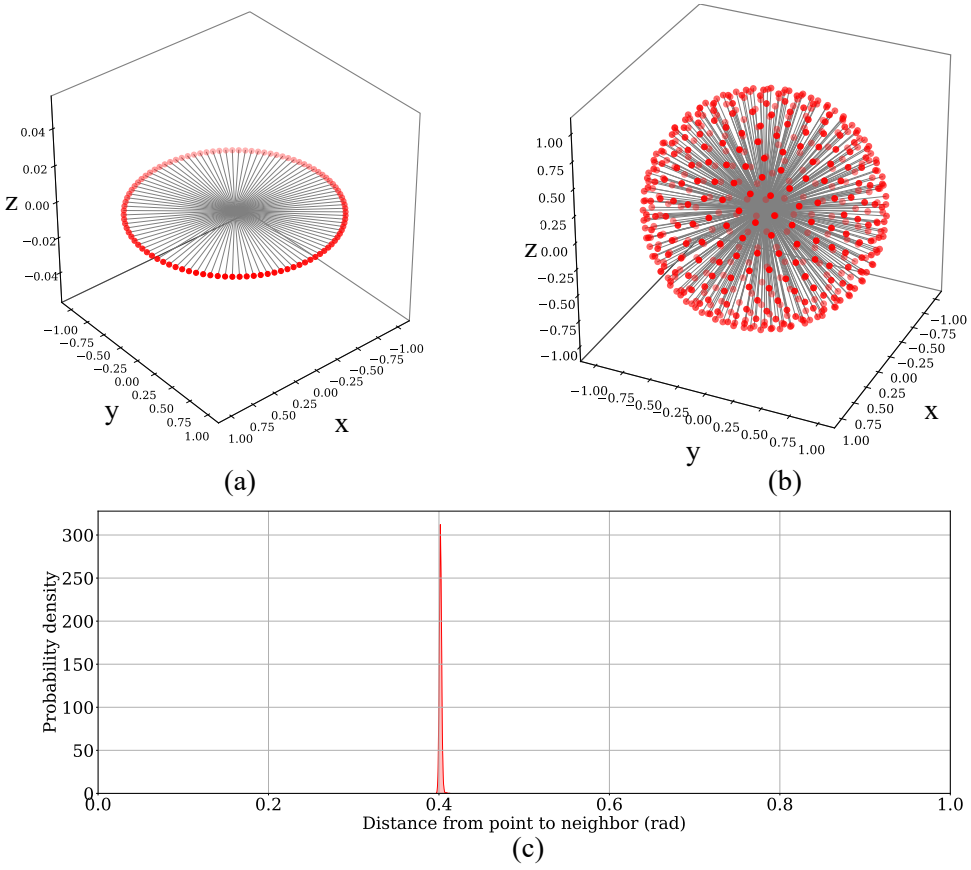

Figure 3. Sampling strategy: (a) 2D circle; (b) 3D sphere; and (c) distribution of distances in 6D

5.2. Model execution stage

The model execution stage refers to the evaluation of the reduced order system of equations that include Eq. (10), Box IV, and the evolution equations for slip, hardening and other internal state variables defined in part-average form. Given the driving macroscopic strain at the current and previous increment, ${}_{l}\bar{\boldsymbol{\epsilon}}$ and ${}_{l+1}\bar{\boldsymbol{\epsilon}}$, and the time increment Δt, the reduced order system of equations are evaluated to update part-wise stresses $\boldsymbol{\sigma}^{(\alpha)}$, separation coefficients $\delta^{(\gamma)}$, and part-average inelastic strain $\boldsymbol{\mu}^{(\alpha)}$ as three sets of unknowns. The ROM execution could be performed as standalone or within a multiscale system, where the ROM is associated with each quadrature point of a macroscopic (i.e., structural) mesh [59, 60]. In the former, the strain and strain rate history $\bar{\boldsymbol{\epsilon}}(t)$ and $\dot{\bar{\boldsymbol{\epsilon}}}(t)$ are treated as known data. In the latter, the macroscale equilibrium process provides the driving strain and time increment, and the same reduced order model can be used for different elements under different loading histories if the underlying microstructure remains unchanged. We have chosen the latter approach, and solve the macroscale equilibrium over one hexahedral element. The ROM is implemented within the commercial finite element code, Abaqus.

A staggered scheme is employed to evaluate the ROM system. The part-average stresses (Eq. (10)) are first solved through a Newton-Raphson process where the separation and inelastic strain coefficients are kept constant at the previous increment values. The separation coefficients are then updated by evaluating the constrained optimization problem (Box IV) with the inelastic strain held at the last increment values and stress coefficients held at the current increment values. The constrained optimization is performed using the COBYLA (constrained optimization by linear approximation) [88] algorithm implemented in the open-source package, NLopt [89]. Finally, the inelastic strain

coefficients are updated by an explicit scheme [68]. The reduced order system evaluation is incorporated into Abaqus using the user supplied subroutine (UMAT) functionality.

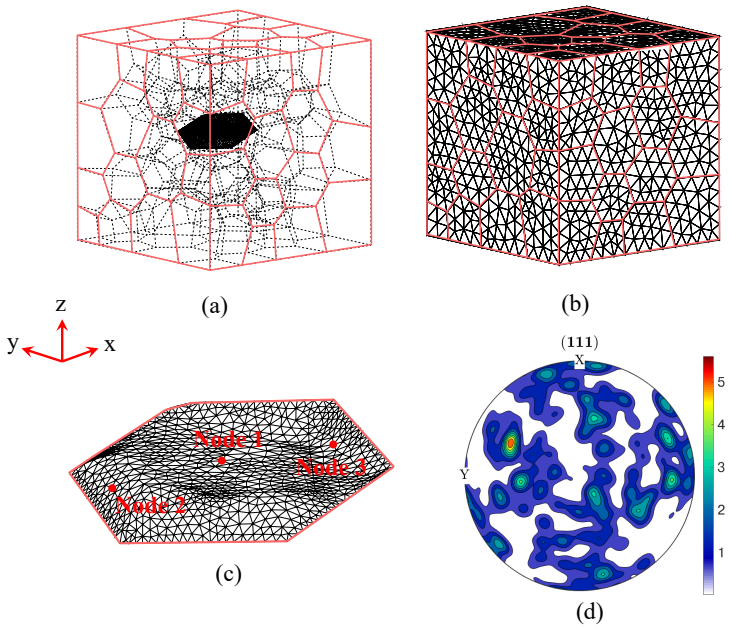

Figure 4. Example set up: (a) crack surface mesh shown in the wireframed polycrystalline microstructure; (b) microstructure mesh; (c) crack surface mesh; and (d) pole figure

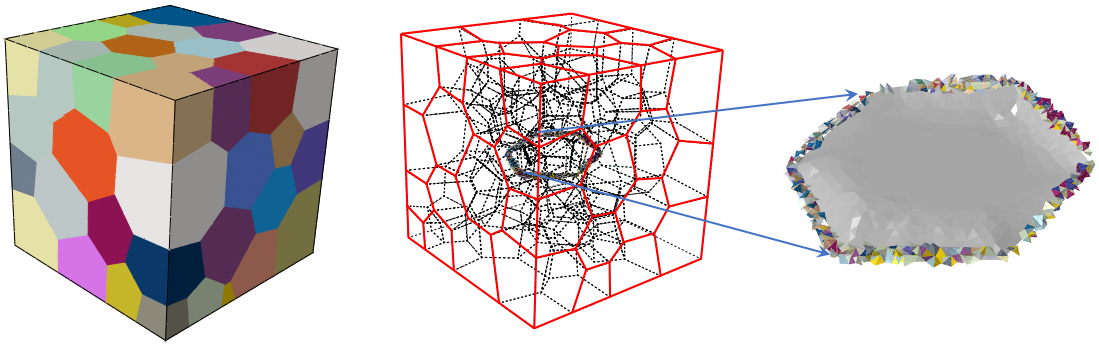

Figure 5. Reduced order partitioning scheme: more ROM parts are defined around the crack front (each color denotes a part)

While this manuscript does not consider parallel implementation strategies, it is possible to parallelize both model training and model execution stages. Model training can be parallelized by splitting the influence function calculations into smaller batches and then submitting each batch to a single compute node. The influence function calculation in each batch are then solved in parallel using all the available processors in a given compute node. For the model execution phase, macroscopic finite element model can be parallelized by partitioning the finite element mesh and then using domain decomposition methods to solve the macroscopic nonlinear finite element problem. For the assembly procedure, one can assign every quadrature point within a domain to a batch of processors where evaluation of the ROM as UMAT stress-update is performed in parallel using the aforementioned batch of processors.

6. Numerical verification

The proposed POD-assisted ROM was verified against direct numerical simulations using CPFE that fully resolve the features of polycrystalline microstructures to characterize the accuracy and efficiency of the proposed model. The microstructures are three dimensional and made up of equiaxed hexagonal close-packed (HCP) crystals. The microstructure domain is discretized using quadratic and linear tetrahedral finite elements that conform to the grain boundaries in the DNS and in the computation of the influence functions, respectively. CPFE simulations with linear elements are known to exhibit locking [25, 31], whereas use of quadratic elements does not offer significant improvement in coefficient tensor computations. A dislocation density-based crystal plasticity model is used to describe the evolution of crystallographic slip and hardening, with model parameters set to represent the behavior of the titanium alloy Ti-6242S. The constitutive equations and the model parameters are described in Refs. [60, 66].

A sample polycrystalline geometry used in the verification studies is shown in Fig. 4(a). This microstructure contains 75 grains and a non-planar crack in the middle of the microstructure. Figures 4(b)-(c) depict the mesh for this microstructure and the crack surface, respectively. The mesh is refined around the crack front, and the total number of elements is 85,645. Figure 4(d) shows the pole figure of the random texture with the grain orientations sampled from a uniform distribution. Examples presented in this study consider a single crack in the microstructure. The presence of multiple short cracks were previously investigated in Ref. [65] in a quasi-2D setting. The present study builds on this foundational framework, but narrows its focus to the effective modeling of a complex 3D crack. As a result, the methodology presented here can be readily extended to address the presence of multiple short cracks.

A POD-assisted EHM model is generated for each microstructure volume using the implementation strategy described in the previous section. The reduced order partitioning for the phase parts is performed using the clustering algorithm as proposed in [65]. The phase partitions of the sample microstructure and a close-up near the crack front are shown in Fig. 5. The parameter n_{space} in the clustering algorithm is set to 150, and the resulting number of phase parts is $n = 228$. More parts are generated by the algorithm near the crack front to better capture the stress and strain concentrations.

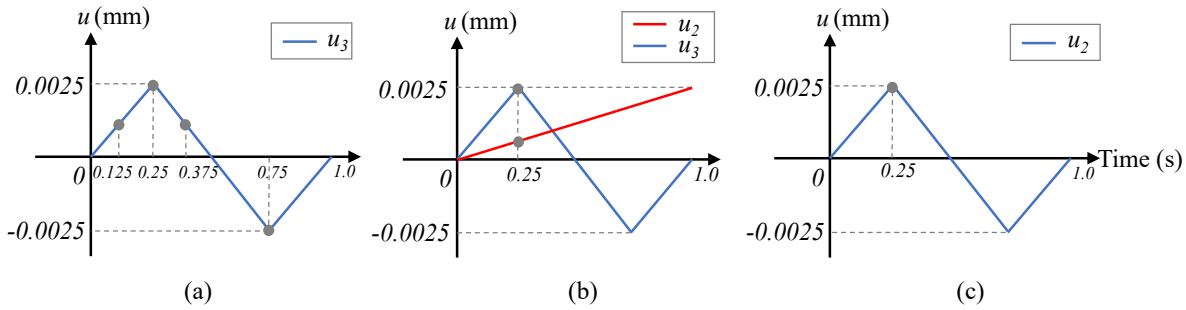

Figure 6. Strain controlled cyclic loadings: (a) uniaxial; (b) biaxial; and (c) simple shear

6.1. Assessment of the snapshot generation strategy

6.1.1. Known loading conditions

In the current example, we make the assumption of a priori knowledge of the external loading orientation, where the known external loading is used to generate the POD basis. The microstructure shown in Fig. 4 is subjected to a strain-controlled cyclic uniaxial loading in z direction shown in Fig. 6(a). The maximum strain applied is 0.25% with R-ratio of -1, and the strain rate is 0.01/s. The boundary condition is shown in Fig. 7(a) for both DNS and ROM (i.e., at model execution stage). Only two external loadings are used as the a priori knowledge: $[\bar{\boldsymbol{\epsilon}}^*]$=[-0.280, -0.252, 0.925, 0.039, -0.013, 0.028] and $[\bar{\boldsymbol{\epsilon}}^*]$=[0.288, 0.253, -0.923, -0.042, 0.0129, 0.004], which are obtained as the normalized, volume-averaged strain values from DNS under 0.25% tension and 0.25% compression, respectively. The corresponding snapshots produced from these two loadings are shown in Fig. 8. The two snapshots were used to generate two POD basis functions (i.e., $n_b = 2$).

The separation fields predicted using the proposed ROM with two separation basis functions are compared to those from the DNS. Figure 9(a) presents the comparison of the separation fields plotted on the base mesh. Contour plots

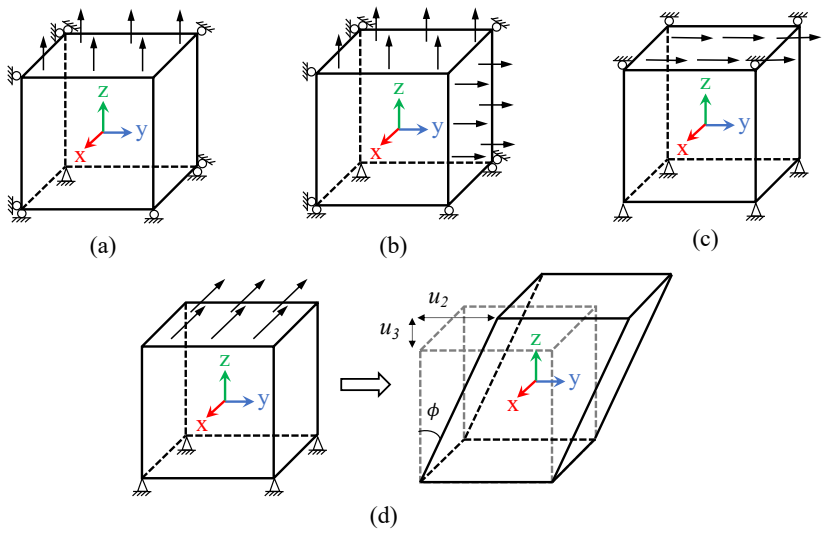

Figure 7. Boundary conditions: (a) for uniaxial loading; (b) for biaxial loading; (c) for simple shear loading; and (d) for combinations of normal and shear loadings

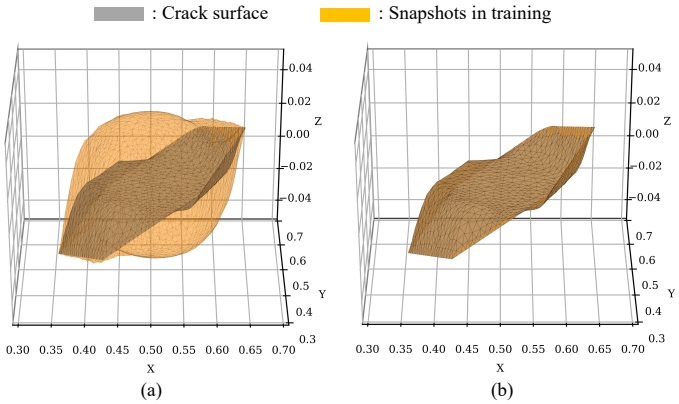

Figure 8. Snapshots generated with a priori knowledge (scale=100): (a) in tension and (b) in compression

of the separation magnitudes $\|\boldsymbol{\delta}(\mathbf{y})\|_2$ and absolute error $\|\boldsymbol{\delta}^{\mathrm{ROM}}(\mathbf{y}) - \boldsymbol{\delta}^{\mathrm{DNS}}(\mathbf{y})\|_2$ between the ROM and DNS are shown in Figs. 9(b) and 9(c), respectively. Employing the relative error measure for the separation field:

$$e = \frac{\|\boldsymbol{\delta}^{\mathrm{DNS}}(\mathbf{y}) - \boldsymbol{\delta}^{\mathrm{ROM}}(\mathbf{y})\|_2}{\|\boldsymbol{\delta}^{\mathrm{DNS}}(\mathbf{y})\|_2} \tag{37}$$

the error at peak tension loading is $e = 10.376\%$. Under the applied cyclic loading magnitudes, the macroscopic stress-strain curve is near linear, although plastic deformation are observed around the crack front (largest plastic strain over 9%). The stiffness of the microstructure is predicted with an error of 1.5%. Figure 10 compares the normal separation-time curves ($\delta_N - t$) at the three selected nodes (1 near the center of the crack and two near the front) shown in Fig. 4(c). The separations predicted by the ROM are slightly smaller than that from the DNS for the three nodes. This difference can be attributed to the stiffer kinematics of the ROM, which provides more resistance to separation as the crack attempts to open. Upon compression, the separation at all three points vanish, demonstrating that the integral form of the constraint used in the ROM is effective in imposing the impenetrability condition.

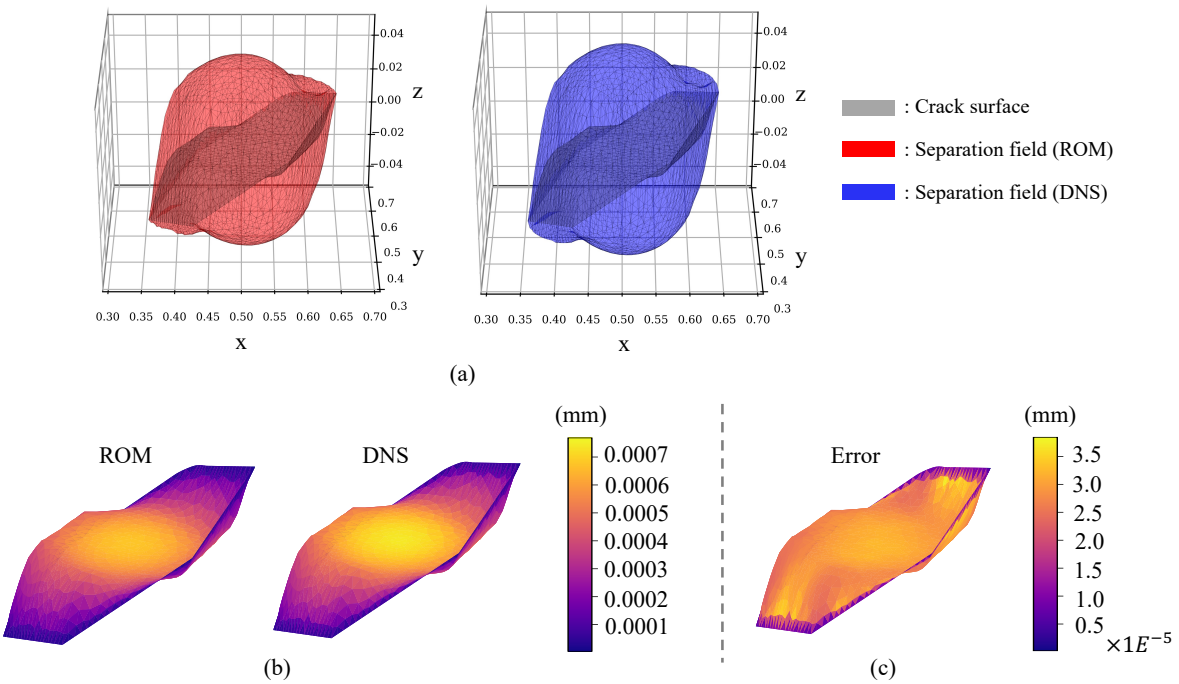

Figure 9. Separation field comparisons at peak separation under cyclic uniaxial loading: (a) actual separation (scale=100); (b) contour plots of the separation magnitudes; and (c) contour plot of the error

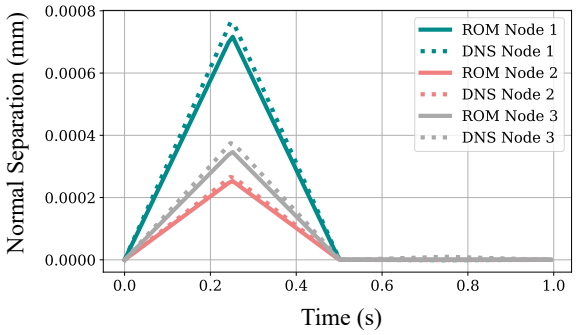

Figure 10. Normal separation-time curves under cyclic uniaxial loading

6.1.2. Uniform snapshot sampling strategy

The sampling strategy described in Section 5.1.1 is assessed when a priori knowledge is absent. Specifically, the effect of the number of snapshots and basis functions on model accuracy is examined using the microstructure shown in Fig. 4. The error measure in Eq. (37) is used for separation field to analyze the performance of the model under monotonic uniaxial tension loading (Fig. 7(a)) and simple shear loading (Fig. 7(c)) at 0.25% strain. The separation basis construction is performed without the information on loading orientation. The results of this analysis are presented in Fig.11(a) and (b) for uniaxial tension loading and simple shear loading, respectively. The figures illustrate the effects of both the number of snapshots, n_{snp}, as well as the number of separation basis functions, n_b. n_{snp} was set to $4, 8, 16, 32, 64$ or 128. For a fixed n_{snp}, the number of basis functions is then raised from 1 to $\min(n_{\text{snp}}, 30)$ to observe the evolution of the model error.

In general, the error decreases as the number of basis functions increases for a fixed number of snapshots. The reduction in error when number of snapshots is increased suggests that the sampling strategy is effective in spanning

the solution space. The errors flatten around 10% for the uniaxial loading and around 20% for the simple shear loading. The residual error is partly attributed to the overly stiff behavior of the ROM as plastic deformation becomes pronounced near the crack front. Increasing the number of reduced order parts would alleviate the stiffness issue to certain extent, but the residual error would still persist, as reported in [65]. This issue is further discussed in Section 6.4.

Increasing the number of snapshots does not always lead to improvement in model accuracy when the number of basis functions is held constant. Two factors contribute to this: the total variance in the training dataset, which increases with more snapshots, and the variance captured by the basis functions, which increases with more basis functions. Fixed basis functions cannot eliminate either of these factors, as the same number of basis functions does not guarantee the same proportion of the total variance captured, and the total variance is also different for different training data. An alternative way to assess the number of snapshots on the ROM's ability to span the solution space and minimize errors is to set the number of basis functions equal to the number of snapshots, $n_b = n_{\text{snp}}$, in which case all variance of the training data can be captured by the basis functions. As highlighted by the solid boxes in Fig. 11, the model accuracy monotonically improves as the number of snapshots increases. For training sets with $n_{\text{snp}} \geq 32$, the maximum number of basis functions used in this study is set to 30 since the error plateaus at number of basis functions less than 30.

In some cases, it is observed that a number of consecutive basis functions do not significantly improve the model accuracy. This is highlighted by the dashed box in Fig. 11, where the model error remains relatively constant as several consecutive basis functions are added, followed by a sudden decrease upon the addition of a single additional basis function. This phenomenon occurs because the error is substantiated under certain loading condition, and some of the basis functions may not be effective at capturing the separation field under this specific loading condition. For instance, Fig. 12 shows the first 6 basis functions computed from the training set with 32 snapshots. It is observed that mode 1 represents opening-dominated deformation while modes 2 and 3 represent shear-dominated deformations (modes 4-6 are more abstract and tend to represent high-dimensional characteristics of the system that are less visually recognizable). The basis functions do not necessarily satisfy contact constraints as discussed in Section 3. Under uniaxial tension loading, the shear-dominated modes such as those shown in Fig. 12(b) and (c) would contribute less to the model accuracy. As a result, the inclusion of these modes leads to the plateaued region observed in Fig. 11(a). Similarly, the incorporation of the normal-dominated modes shown in Fig. 12(a) leads to the plateaued region seen in Fig. 11(b). The non-smooth trend of the curves in Fig. 11 can also be attributed to the same underlying cause.

In a general setting, it is important to define selection criteria for the number of basis functions for a given number of snapshots, as well as for the number of snapshots. For a fixed number of snapshots, the number of basis functions are selected based on the total variance captured from the training data. In POD, the basis functions are derived using the eigenvectors identified via singular value decomposition. The sum of magnitudes of the corresponding eigenvalues indicate the percentage of total variance that the associated eigenvectors can explain [90]. The number of basis functions are decided by specifying a desired level of explained variance. In the present example, we selected this value to be 99%, which corresponds to 18 basis functions when number of snapshots are fixed at 32. We note that the value of 99% ensures that for any given number of snapshots in Fig. 11, the errors have reached their low steady-state values. The number of snapshots are selected such that the solution space is spanned to a desired level of accuracy. The spanning of the solution space is related to the uniform sampling strategy over the 6-dimensional unit sphere (Section 5.1.1). The resultant average distance between any point on the surface of the hypersphere and its neighboring points, is an indicator of how well this space is spanned. In the present example, we use the Euclidean distance between two neighboring points as the distance measure and select this value to be around 0.8, which corresponds to 32 snapshots. Figure 11(c) shows the variation of the distance measure as a function of the number of snapshots. The selected distance measure is near the elbow point of the nonlinear curve, indicating that increasing the number of snapshots do not significantly reduce the distance measure. It is worth noting that the selection procedures are performed during the model training phase i.e., no reference simulation is required.

6.2. Model accuracy under different loading conditions

The microstructure shown in Fig. 4 was subjected to a number of additional loading conditions. The separation basis is constructed using a total of 32 snapshots, generated through the uniform sampling strategy. The first 18 basis functions are used in the ROM.

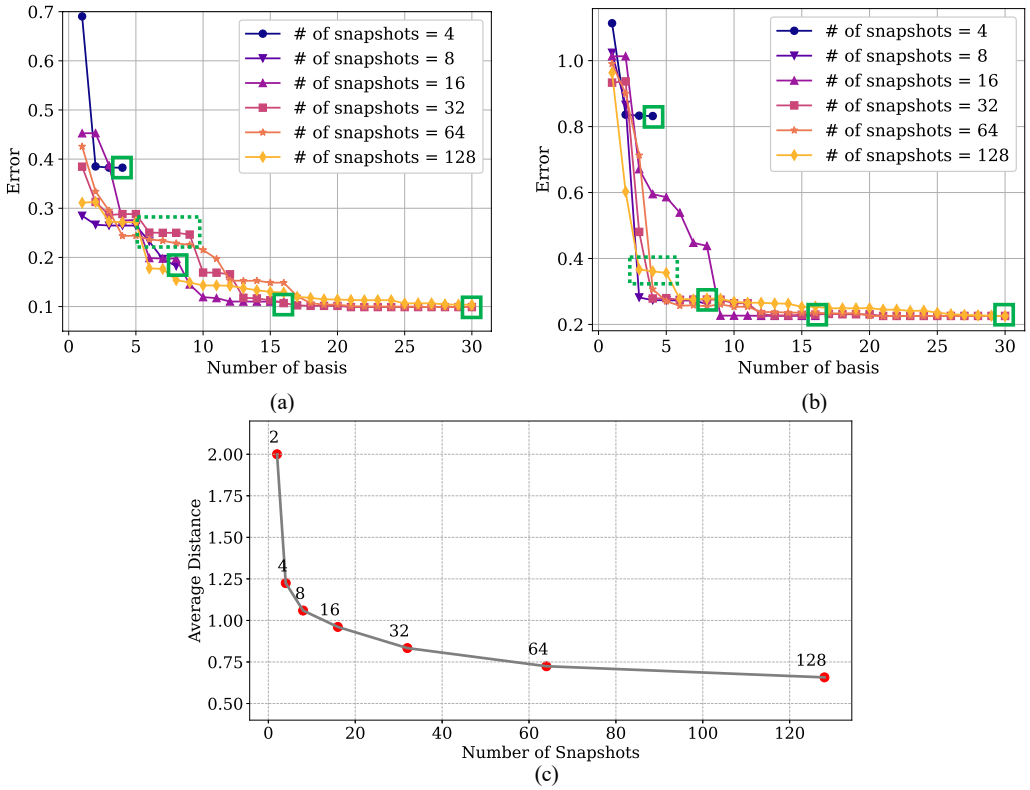

Figure 11. Error as a function of number of snapshots and basis functions: (a) under uniaxial tension; and (b) under simple shear. Evolution of the distance between two sampling points in the strain space as a function of number of snapshots shown in (c).

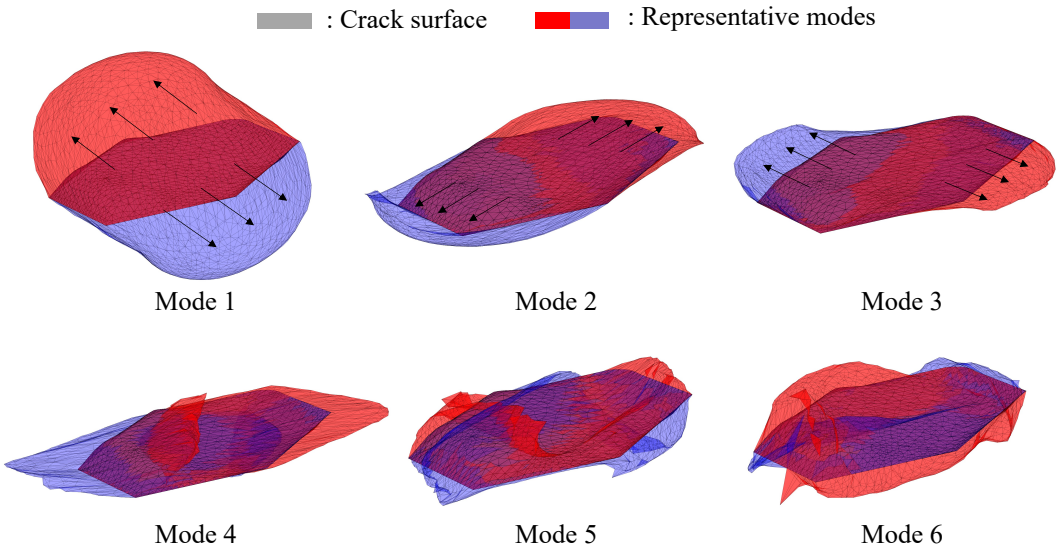

Figure 12. Representative modes (red is upper surface, blue is lower surface) plotted on the crack surface (gray): The arrows in Modes 1-3 denote the general crack opening direction; Modes 4-6 represent high-dimensional characteristics of the system and are more abstract

When the microstructure is subjected to the same cyclic uniaxial loading (Fig. 7(a)), the model accuracy is comparable to the case in which a priori knowledge is applied (Section 6.1). The error of the separation at the peak tension is $e = 10.403\%$. The microstructure is then subjected to the strain controlled biaxial loading shown in Fig. 6(b) and the boundary conditions in Fig. 7(b). The microstructure is loaded in the z direction cyclically with applied strain up to 0.25% with R-ratio $= -1$ at constant strain rate of 0.01/s. Simultaneously, a 0.25% uniaxial and monotonic tensile strain is applied with a constant strain rate of 0.0025/s in the y direction. The model comparisons are shown in Fig. 13. The contour plots are extracted at the tensile peak of cyclic load as marked in Fig 6(b). In general, reasonable agreements are observed between the ROM and DNS for both separation field and stress-strain comparisons. The error of the separation is $e = 9.010\%$ at the marked load state. Figure 14 shows the same comparisons subjected to the strain controlled simple shear loading in Fig. 6(c) and the boundary conditions in Fig. 7(c). The microstructure is loaded in the y direction cyclically with applied strain up to 0.25% with R-ratio $= -1$ at constant strain rate of 0.01/s. The separation field plotted is in the sliding direction. The separation discrepancy between ROM and DNS in this case is larger than those from the previous two loading conditions. The error of the separation is $e = 22.452\%$ at the time step marked in Fig. 6(c). In all loading conditions, the ROM predicts a slightly smaller separation compared with the DNS.

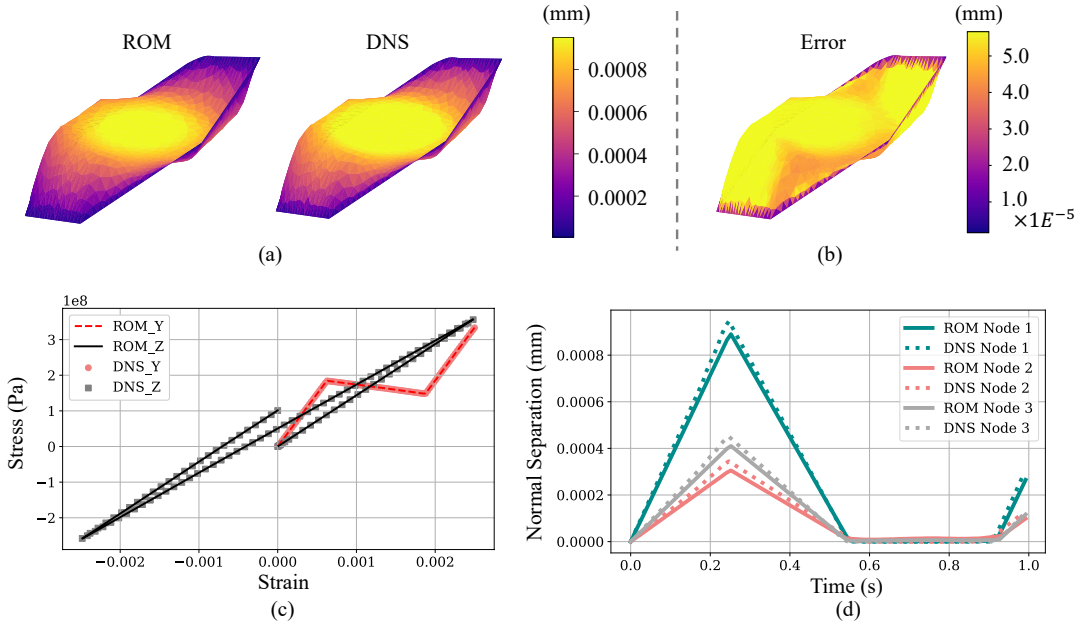

Figure 13. Under cyclic biaxial loading: (a) contour plots of separation fields at peak separation; (b) contour plot of absolute error; (c) engineering stress-strain curves; and (d) separation-time curves for selected nodes

The reduced order model is further verified under multiaxial loading conditions generated using the boundary conditions shown in Fig. 7(d). The microstructure is loaded monotonically along the y-z plane up to 0.25% strain magnitude. Figure 15 shows the normal separation as a function of different loadings for the selected three nodes in Fig. 4(c), which is constructed by varying the magnitudes of u_3 and u_2 to account for various normal and shear strain combinations with proportional loading, and then observing the evolution of the normal separation δ_N as predicted by the ROM and DNS. The combinations of u_3 and u_2 are generated using: $u_3 = 0.0025\cos(\pi/2(n_{\text{load}}-1)i)$ and $u_2 = 0.0025\sin(\pi/2(n_{\text{load}}-1)i)$, where n_{load} is the total number of load cases (n_{load}=10), and $i = 0, ..., n_{\text{load}}-1$. Under all loading conditions and for all three selected nodes, the ROM shows reasonable match with the DNS.

6.3. Model efficiency

To evaluate the model efficiency, the microstructure in Fig. 4 is subjected to cyclic uniaxial loading up to 0.25% strain, and the model order reduction scheme is the same as that of the previous example ($n = 228$; $n_b = 18$). Each model is executed for three times using the same machine with a single core, and the average run time is recorded.

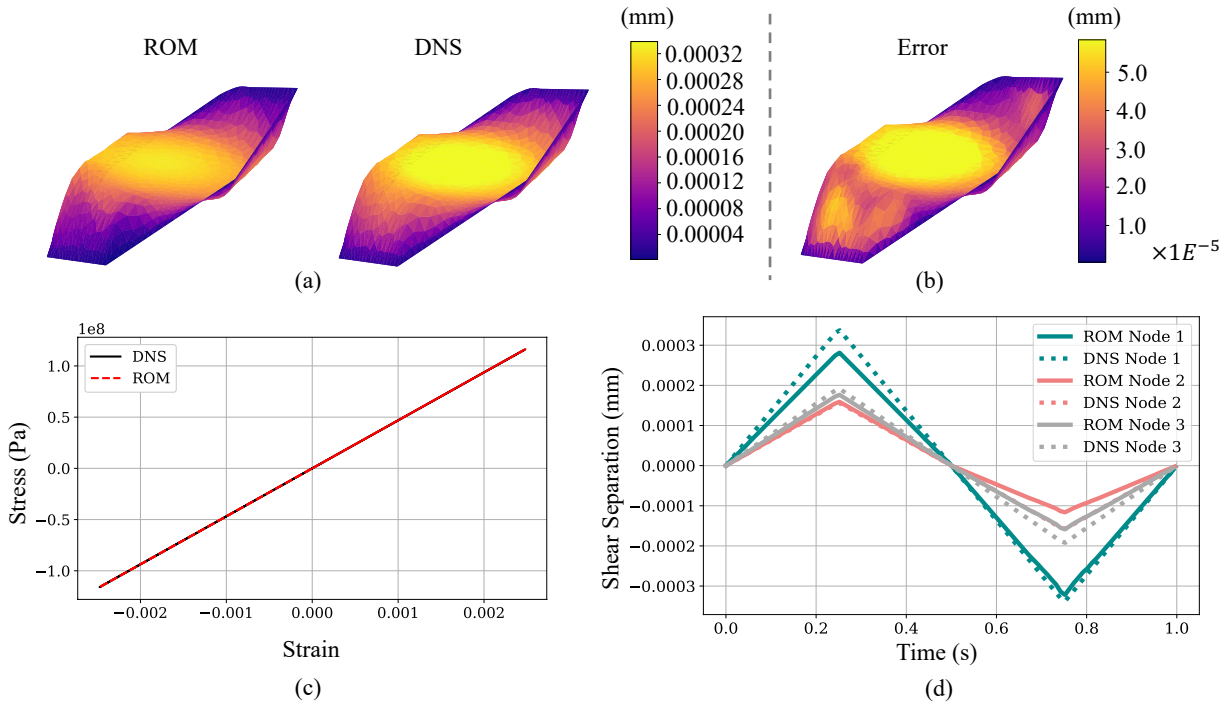

Figure 14. Under cyclic simple shear loading: (a) contour plots of separation fields at peak separation; (b) contour plot of absolute error; (c) engineering stress-strain curves; and (d) separation-time curves for selected nodes

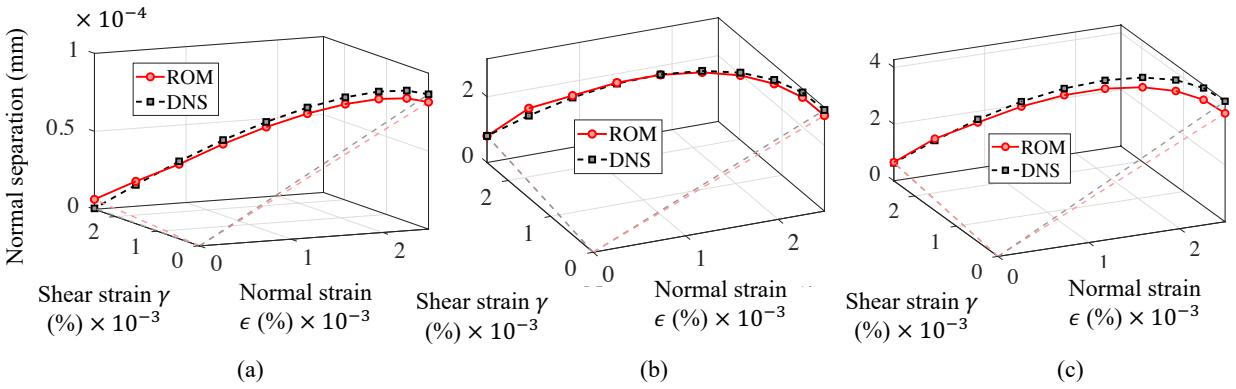

Figure 15. Peak normal separation under different combinations of normal and shear loadings: (a) node 1; (b) node 2; and (c) node 3

There are 105 increments in both of the ROM and DNS simulations. The ROM exhibits a significant improvement in computational efficiency (68.43 s) compared with the DNS simulation (18,547.57 s). The speedup is around 271, which is of the same orders of magnitude as previously reported for EHM [59, 61]. The same level of the speedup can be attributed to the efficient implementation of the constrained optimization problem. In the present example, when the impenetrability constraint is not activated, such as under tension, solving the stress equations alone takes up more than 99% of the total computational run time. On the other hand, when the impenetrability constraint is in effect, the computational time distributed among stress equations, constrained optimization equations and evolution equations are 41.5%, 58.1%, and 0.4% of the total run time, respectively. Therefore, the computational costs of solving the constrained optimization equations is comparable to solving the stress equations even with complex crack morphologies.

6.4. Assessment of local stress/strain response and effect of load amplitude

In this section, we assess ROM's ability to capture the localized stress/strain behavior. Even when the overall stress-strain behavior remains linear, crack front regions may exhibit elasto-plastic deformations. Figure 16 compares the phase part-averaged von Mises stress and maximum principal strain for the microstructure under the cyclic uniaxial loadings with peak applied strain of 0.25%. In the CPFE simulations, the response fields were averaged within subdomains of each phase part for one-to-one comparisons. In Fig. 16, the parts near the crack front (as defined in Fig. 4) are highlighted with markers. It is evident that these highlighted parts experience high local stress and strain values compared with other regions of the microstructure and exhibit viscoplastic behavior. The DNS exhibits a slightly softer behavior, with slightly smaller local stresses and larger local strains.

Figures 17(a) and (b) present the same comparisons, but when the load amplitude is doubled to an applied maximum strain of 0.5%. As shown in Fig. 17(a), there is a substantial increase in stress/strain magnitudes. The errors in part-averaged local stress and strain are larger compared with the 0.25% strain case. The separation discrepancy, as demonstrated in Fig. 17(c), is also larger compared to the small strain case (see Fig. 10 (d)). The error of the separation field at peak tension is increased to $e = 21.223\%$. The reduction of ROM accuracy with increased load amplitude is primarily attributed to two reasons: (i) As the plastic deformation near the crack front increases, the crack front opening displacements get larger and a more blunted separation profile occurs. The snapshots generated by the linear elastic analysis does not account for this blunting, and therefore the resulting basis functions cannot approximate them with as high an accuracy, resulting in higher error in the separation fields. It may be possible to use a similar approach as proposed in [71, 72], where the space of snapshots is constructed directly from CPFE analysis where the elastoplastic behavior is considered. This approach would significantly increase training cost. (ii) Overly stiff behavior observed due to the locking phenomenon induced by the increased instantaneous modulus contrast between plastically flowing and elastically deforming parts in the microstructure. This issue has been studied in [91, 92] particularly for low-order ROMs, but has yet to be addressed in the context of polycrystalline microstructures.

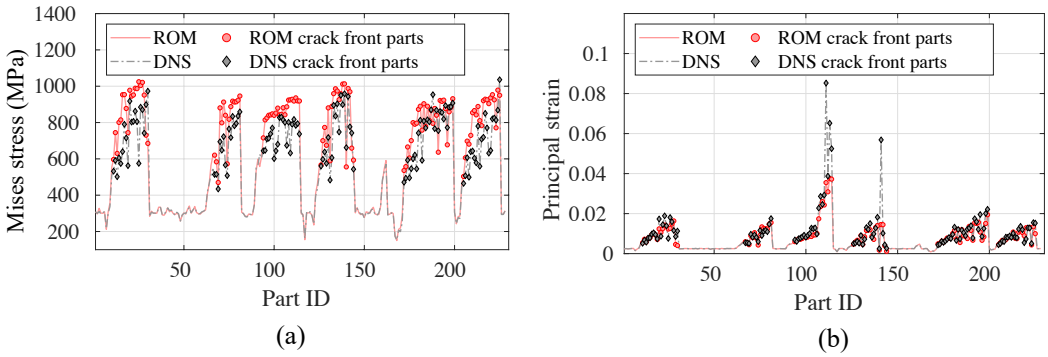

Figure 16. Grain-averaged stress and strain comparisons under 0.25% strain

6.5. Effect of crack morphology

In this section, the ROM is further verified by considering a different and more complex crack morphology that has been observed in experiments. Pilchak [8] directly examined fractured samples of single-phase Ti–7Al subjected to cyclic and dwell fatigue loading. Two mechanisms of crack growth were identified: (i) faceted mode (Fig. 18(a)), when the crack is propagating through hard-oriented grains via $\langle c + a \rangle$ slip mechanism; and (ii) striation mode (Fig. 18(b)), when the crack is propagating through soft-oriented grains via prism $\langle a \rangle$ slip mechanisms. It is possible for the crack to undergo a transition in mode of propagation when it traverses hard-soft grain pairs. As shown in Fig 18(c), the overall crack growth direction is from left to right. One can see the crack surface starts with faceted growth, after which a grain boundary is encountered and the crack mode switches to striation growth. In the current study, we reconstruct the crack morphology when transition of crack modes occurs. The resulting reconstructed crack morphology is illustrated in Fig. 18(d).

The microstructure and mesh in Fig. 4(a) and (b) is used to construct the example. The polycrystalline volume containing the crack and the crack surface mesh is shown in Fig. 19(a) and (b), respectively. The total number of

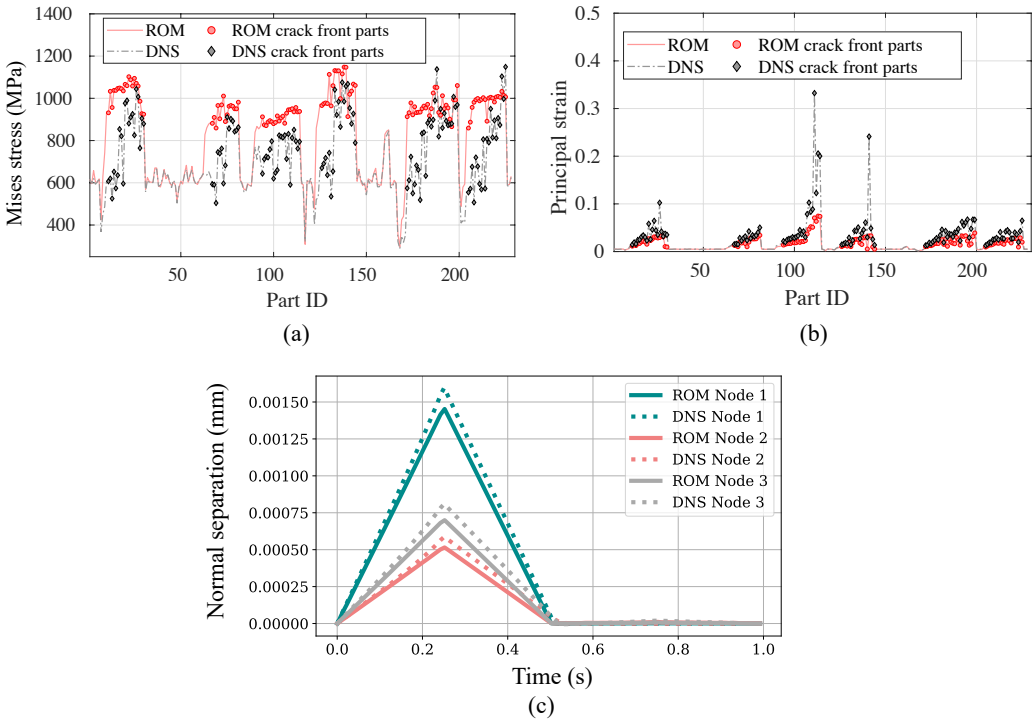

Figure 17. (a) Grain-averaged stress comparisons; (b) grain-averaged strain comparisons; and (c) normal separation-time curves for the selected three nodes under 0.5% strain

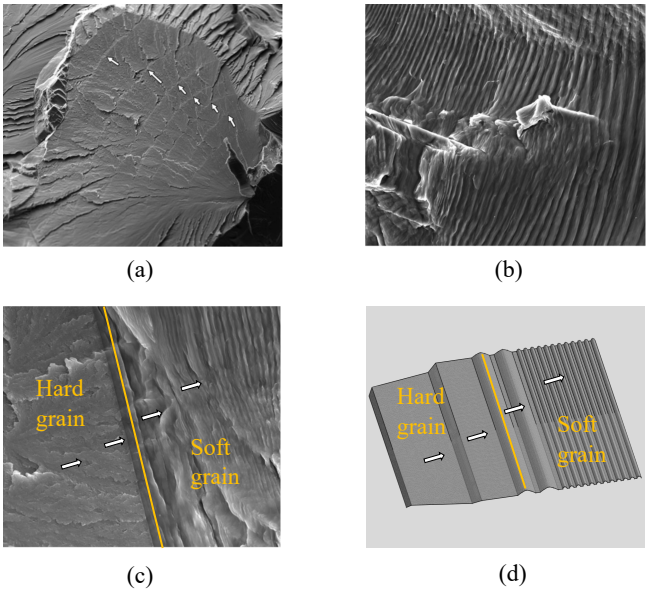

Figure 18. Crack growth modes reproduced from [8]: (a) Faceted growth mode; (b) striation growth mode; (c) transition of modes; and (d) reconstructed crack morphology

elements is 79,730. The number of reduced order parts is $n = 265$ with $n_{\text{space}} = 100$. A total of 18 basis functions are generated from 32 snapshots. The microstructure is subjected to cyclic uniaxial tension up to 0.25% strain. The

separation fields are compared at the four marked stages in Fig. 6(a). Only one increment in compression is selected since there is no discernible difference of the separation field during the crack closure. The results are shown in Fig. 20. A reasonable match between the contour plots of ROM and DNS is observed at all four stages. Following the previous verification examples, the ROM slightly underestimates the separation due to more rigid kinematics.

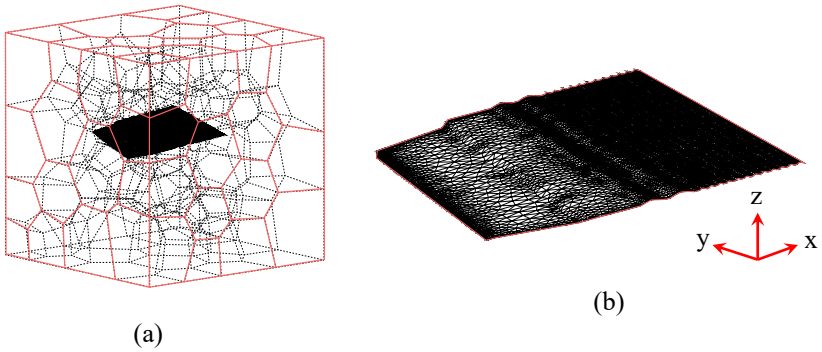

Figure 19. (a) Polycrystalline volume containing the reconstructed crack; (b) meshing of the reconstructed crack

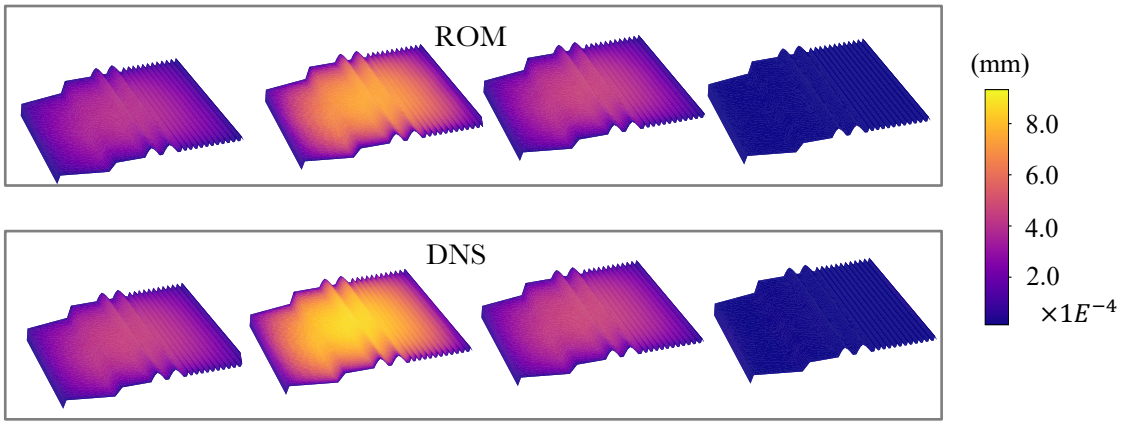

Figure 20. Separation contours comparison at four selected stages

7. Conclusions and future works

This manuscript proposes a novel reduced order homogenization model to predict the mechanical response of full-3D polycrystalline microstructure in the presence of tortuous cracks. The proposed approach reformulates the EHM framework with the assistance of POD to account for the local crystal plasticity and the presence of tortuous cracks. The reduced order system of equations for separation are reformulated as a constrained optimization problem with an integrated form of constraint such that the computational efficiency of EHM is retained. The proposed model is verified through comparisons with direct numerical simulations employing crystal plasticity as the constitutive relation. The model is evaluated under three different cyclic loading conditions and a combination of monotonic tension and shear loadings, and shows good agreement with DNS results for the separation field, overall stress-strain, and local stress and strain predictions. The model is tested under a random textured microstructure with two different crack configurations including one reconstructed from the experiments. The ROM show a reasonable error level of around 10% on both of the examples. The model demonstrates a significant improvement in computational efficiency due to the efficient implementation of the constrained optimization problem such that the time required to enforce the impenetrability constraint does not substantially contribute to the overall computational runtime.

To extend the capabilities of the current work, addressing the degradation of model performance with increasing crack tip plastic deformation is necessary. The results presented in this manuscript demonstrate that the crack separation field predictions, which rely on separation basis functions constructed through linear elastic simulations, begin to deviate from direct numerical simulation predictions at high levels of local plastic strain. On the other hand, employing nonlinear analysis to build more accurate basis functions increases the computational cost of model training significantly. An idea is to add training data from simulations that include plasticity exclusively around the crack tip region. This approach could improve model accuracy while limiting the added computational costs in the training stage.

The proposed model could also be extended to account for the growth of MSCs, particularly under cyclic loading conditions. Recent work points to significant computational costs [9] associated with tracking growth of 3D cracks in polycrystalline materials given their morphological complexity. This computational cost issue could be partially alleviated by using the proposed ROM approach. Modeling crack growth also raises the natural question of transition from short crack to long crack growth regime, and the consistent transition of the pertinent growth models. The stress and deformation states predicted by the current approach do not depend on crack size, provided that the crack tips are sufficiently far from the boundaries [65] Therefore, the ROM predicts the mechanical state for long cracks as well. However, direct representation of the grain scale features is likely to have a minor impact in the long crack growth regime since crack growth does not significantly depend on local texture.

8. Acknowledgements

The authors gratefully acknowledge the financial support from the National Aeronautics and Space Administration (NASA), Space Technology Early State Innovation (ESI) Grant (No.:80NSS C20K0294).

References

[1] K. Miller, R. Akid, The application of microstructural fracture mechanics to various metal surface states, Proceedings of the Royal Society of London. Series A: Mathematical, Physical and Engineering Sciences 452 (1949) (1996) 1411–1432.
[2] H.-J. Christ, O. Düber, C.-P. Fritzen, H. Knobbe, P. Köster, U. Krupp, B. Künkler, Propagation behaviour of microstructural short fatigue cracks in the high-cycle fatigue regime, Computational materials science 46 (3) (2009) 561–565.
[3] K. Sadananda, M. N. Babu, A. Vasudevan, A review of fatigue crack growth resistance in the short crack growth regime, Materials Science and Engineering: A 754 (2019) 674–701.
[4] K. Hussain, Short fatigue crack behaviour and analytical models: a review, Engineering Fracture Mechanics 58 (4) (1997) 327–354.
[5] T. Zhai, A. Wilkinson, J. Martin, A crystallographic mechanism for fatigue crack propagation through grain boundaries, Acta Materialia 48 (20) (2000) 4917–4927.
[6] T. Zhai, X. Jiang, J. Li, M. Garratt, G. Bray, The grain boundary geometry for optimum resistance to growth of short fatigue cracks in high strength al-alloys, International Journal of Fatigue 27 (10-12) (2005) 1202–1209.
[7] M. Herbig, A. King, P. Reischig, H. Proudhon, E. M. Lauridsen, J. Marrow, J.-Y. Buffière, W. Ludwig, 3-d growth of a short fatigue crack within a polycrystalline microstructure studied using combined diffraction and phase-contrast x-ray tomography, Acta Materialia 59 (2) (2011) 590–601.
[8] A. L. Pilchak, Fatigue crack growth rates in alpha titanium: faceted vs. striation growth, Scripta Materialia 68 (5) (2013) 277–280.
[9] H. Proudhon, J. Li, W. Ludwig, A. Roos, S. Forest, Simulation of short fatigue crack propagation in a 3d experimental microstructure, Advanced Engineering Materials 19 (8) (2017) 1600721.
[10] A. Rovinelli, M. D. Sangid, H. Proudhon, Y. Guilhem, R. A. Lebensohn, W. Ludwig, Predicting the 3d fatigue crack growth rate of small cracks using multimodal data via bayesian networks: In-situ experiments and crystal plasticity simulations, Journal of the Mechanics and Physics of Solids 115 (2018) 208–229.
[11] D. Peirce, R. Asaro, A. Needleman, An analysis of nonuniform and localized deformation in ductile single crystals, Acta Metallurgica 30 (6) (1982) 1087–1119.
[12] D. Peirce, R. J. Asaro, A. Needleman, Material rate dependence and localized deformation in crystalline solids, Acta Metallurgica 31 (12) (1983) 1951–1976.
[13] M. Knezevic, B. Drach, M. Ardeljan, I. J. Beyerlein, Three dimensional predictions of grain scale plasticity and grain boundaries using crystal plasticity finite element models, Computer Methods in Applied Mechanics and Engineering 277 (2014) 239–259.
[14] V. T. Phan, X. Zhang, Y. Li, C. Oskay, Microscale modeling of creep deformation and rupture in nickel-based superalloy IN 617 at high temperature, Mech. Mater. 114 (2017) 215–227.
[15] Y. Liu, Y. Zhu, C. Oskay, P. Hu, L. Ying, D. Wang, Experimental and computational study of microstructural effect on ductile fracture of hot-forming materials, Mater. Sci. Eng. A 724 (2018) 298–323.
[16] Y. Liu, X. Zhang, C. Oskay, A comparative study on fatigue indicator parameters for near- titanium alloys, Fatigue Fract Eng Mater Struct. 46 (2023) 271–294.
[17] N. Jezernik, J. Kramberger, T. Lassen, S. Glodež, Numerical modelling of fatigue crack initiation and growth of martensitic steels, Fatigue & Fracture of Engineering Materials & Structures 33 (11) (2010) 714–723.

[18] B. Lin, L. Zhao, J. Tong, A crystal plasticity study of cyclic constitutive behaviour, crack-tip deformation and crack-growth path for a polycrystalline nickel-based superalloy, Engineering Fracture Mechanics 78 (10) (2011) 2174–2192.
[19] E. Mikkola, G. Marquis, J. Solin, Mesoscale modelling of crack nucleation from defects in steel, International Journal of Fatigue 41 (2012) 64–71.
[20] J. Li, H. Proudhon, A. Roos, V. Chiaruttini, S. Forest, Crystal plasticity finite element simulation of crack growth in single crystals, Computational Materials Science 94 (2014) 191–197.
[21] H. Proudhon, J. Li, F. Wang, A. Roos, V. Chiaruttini, S. Forest, 3d simulation of short fatigue crack propagation by finite element crystal plasticity and remeshing, International Journal of Fatigue 82 (2016) 238–246.
[22] B. R. Phung, A. D. Spear, A voxel-based remeshing framework for the simulation of arbitrary three-dimensional crack growth in heterogeneous materials, Engineering Fracture Mechanics 209 (2019) 404–422.
[23] F. Briffod, T. Shiraiwa, M. Enoki, Nucleation and propagation modeling of short fatigue crack in rolled bi-modal ti–6al–4v alloy, Materials Science and Engineering: A 790 (2020) 139710.
[24] D. Zhu, W. Zhang, Z. Ding, A multiscale crack iteration and remeshing model for low-cycle crack propagation evaluation, Journal of Engineering Mechanics 148 (8) (2022) 04022039.
[25] J. Cheng, A. Shahba, S. Ghosh, Stabilized tetrahedral elements for crystal plasticity finite element analysis overcoming volumetric locking, Computational Mechanics 57 (2016) 733–753.
[26] M. Diehl, M. Wicke, P. Shanthraj, F. Roters, A. Brueckner-Foit, D. Raabe, Coupled crystal plasticity–phase field fracture simulation study on damage evolution around a void: pore shape versus crystallographic orientation, Jom 69 (2017) 872–878.
[27] T.-T. Nguyen, J. Réthoré, J. Yvonnet, M. C. Baietto, Multi-phase-field modeling of anisotropic crack propagation for polycrystalline materials, Computational Mechanics 60 (2017) 289–314.
[28] A. Sadeghirad, K. Momeni, Y. Ji, X. Ren, L. Chen, J. Lua, Multiscale crystal-plasticity phase field and extended finite element methods for fatigue crack initiation and propagation modeling, International Journal of Fracture 216 (2019) 41–57.
[29] X. Tu, A. Ray, S. Ghosh, A coupled crystal plasticity fem and phase-field model for crack evolution in microstructures of 7000 series aluminum alloys, Engineering Fracture Mechanics 230 (2020) 106970.
[30] J. Cheng, X. Tu, S. Ghosh, Wavelet-enriched adaptive hierarchical fe model for coupled crystal plasticity-phase field modeling of crack propagation in polycrystalline microstructures, Computer Methods in Applied Mechanics and Engineering 361 (2020) 112757.
[31] W. G. Feather, H. Lim, M. Knezevic, A numerical study into element type and mesh resolution for crystal plasticity finite element modeling of explicit grain structures, Computational Mechanics 67 (2021) 33–55.
[32] A. Emdadi, M. A. Zaeem, Phase-field modeling of crack propagation in polycrystalline materials, Computational Materials Science 186 (2021) 110057.
[33] M. C. Baietto, E. Pierres, A. Gravouil, B. Berthel, S. Fouvry, B. Trolle, Fretting fatigue crack growth simulation based on a combined experimental and xfem strategy, International Journal of Fatigue 47 (2013) 31–43.
[34] V. Wan, D. MacLachlan, F. Dunne, Integrated experiment and modelling of microstructurally-sensitive crack growth, International Journal of Fatigue 91 (2016) 110–123.
[35] F. Farukh, L. Zhao, R. Jiang, P. Reed, D. Proprentner, B. Shollock, Realistic microstructure-based modelling of cyclic deformation and crack growth using crystal plasticity, Computational Materials Science 111 (2016) 395–405.
[36] D. Wilson, Z. Zheng, F. P. Dunne, A microstructure-sensitive driving force for crack growth, Journal of the Mechanics and Physics of Solids 121 (2018) 147–174.
[37] D. Wilson, F. P. Dunne, A mechanistic modelling methodology for microstructure-sensitive fatigue crack growth, Journal of the Mechanics and Physics of Solids 124 (2019) 827–848.
[38] D. Wilson, W. Wan, F. P. Dunne, Microstructurally-sensitive fatigue crack growth in hcp, bcc and fcc polycrystals, Journal of the Mechanics and Physics of Solids 126 (2019) 204–225.
[39] P. Zhang, L. Zhang, K. Baxevanakis, L. Zhao, C. Bullough, Modelling short crack propagation in a single crystal nickel-based superalloy using crystal plasticity and xfem, International Journal of Fatigue 136 (2020) 105594.
[40] J. Mao, Y. Xu, D. Hu, X. Liu, J. Pan, H. Sun, R. Wang, Microstructurally short crack growth simulation combining crystal plasticity with extended finite element method, Engineering Fracture Mechanics 275 (2022) 108786.
[41] V. Karamitros, D. W. MacLachlan, F. P. Dunne, Mechanistic fatigue in ni-based superalloy single crystals: A study of crack paths and growth rates, Journal of the Mechanics and Physics of Solids 158 (2022) 104663.
[42] X. Zhang, F. P. Dunne, 3d cp-xfem modelling of short crack propagation interacting with twist/tilt nickel grain boundaries, Journal of the Mechanics and Physics of Solids 168 (2022) 105028.
[43] V. Karamitros, D. W. MacLachlan, F. P. Dunne, Modelling of short crack growth in single crystal ni γ- γ microstructure, Acta Materialia 240 (2022) 118305.
[44] Z. Cheng, H. Wang, P. Wang, A multi-grid sampling multi-scale method for crack initiation and propagation, Engineering Fracture Mechanics 271 (2022) 108671.
[45] T. Luther, C. Könke, Polycrystal models for the analysis of intergranular crack growth in metallic materials, Engineering Fracture Mechanics 76 (15) (2009) 2332–2343.
[46] M. Lu, F. Wang, X. Zeng, W. Chen, J. Zhang, Cohesive zone modeling for crack propagation in polycrystalline niti alloys using molecular dynamics, Theoretical and Applied Fracture Mechanics 105 (2020) 102402.
[47] N. Weinzapfel, F. Sadeghi, Numerical modeling of sub-surface initiated spalling in rolling contacts, Tribology International 59 (2013) 210–221.
[48] A. Prakash, R. Lebensohn, Simulation of micromechanical behavior of polycrystals: finite elements versus fast fourier transforms, Modelling and Simulation in Materials Science and Engineering 17 (6) (2009) 064010.
[49] A. Rovinelli, H. Proudhon, R. A. Lebensohn, M. D. Sangid, Assessing the reliability of fast fourier transform-based crystal plasticity simulations of a polycrystalline material near a crack tip, International Journal of Solids and Structures 184 (2020) 153–166.
[50] R. Ma, W. Sun, Fft-based solver for higher-order and multi-phase-field fracture models applied to strongly anisotropic brittle materials,

Computer Methods in Applied Mechanics and Engineering 362 (2020) 112781.
[51] S. Lucarini, F. P. Dunne, E. Martínez-Pañeda, An fft-based crystal plasticity phase-field model for micromechanical fatigue cracking based on the stored energy density, International Journal of Fatigue 172 (2023) 107670.
[52] A. Vidyasagar, W. L. Tan, D. M. Kochmann, Predicting the effective response of bulk polycrystalline ferroelectric ceramics via improved spectral phase field methods, Journal of the Mechanics and Physics of Solids 106 (2017) 133–151.
[53] J. Oliver, M. Caicedo, A. E. Huespe, J. Hernández, E. Roubin, Reduced order modeling strategies for computational multiscale fracture, Computer Methods in Applied Mechanics and Engineering 313 (2017) 560–595.
[54] J. Oliver, D. L. Linero, A. E. Huespe, O. L. Manzoli, Two-dimensional modeling of material failure in reinforced concrete by means of a continuum strong discontinuity approach, Computer Methods in Applied Mechanics and Engineering 197 (5) (2008) 332–348.
[55] Z. Liu, Deep material network with cohesive layers: multi-stage training and interfacial failure analysis, Computer Methods in Applied Mechanics and Engineering 363 (2020) 112913.
[56] C. Oskay, J. Fish, Eigendeformation-based reduced order homogenization for failure analysis of heterogeneous materials, Computer Methods in Applied Mechanics and Engineering 196 (7) (2007) 1216–1243.
[57] Z. Yuan, J. Fish, Multiple scale eigendeformation-based reduced order homogenization, Computer Methods in Applied Mechanics and Engineering 198 (21-26) (2009) 2016–2038.
[58] C. Oskay, G. Pal, A multiscale failure model for analysis of thin heterogeneous plates, Int. J. Damage Mechanics 19 (2010) 575–611.
[59] X. Zhang, C. Oskay, Eigenstrain based reduced order homogenization for polycrystalline materials, Computer Methods in Applied Mechanics and Engineering 297 (2015) 408–436.
[60] Y. Liu, X. Zhang, Y. Zhu, P. Hu, C. Oskay, Dislocation density informed eigenstrain based reduced order homogenization modeling: verification and application on a titanium alloy structure subjected to cyclic loading, Modelling and Simulation in Materials Science and Engineering 28 (2) (2020) 025004.
[61] D. Xia, X. Zhang, C. Oskay, Large-deformation reduced order homogenization of polycrystalline materials, Computer Methods in Applied Mechanics and Engineering 387 (2021) 114119.
[62] Z. Yuan, J. Fish, Are the cohesive zone models necessary for delamination analysis?, Computer Methods in Applied Mechanics and Engineering 310 (2016) 567–604.
[63] C. Oskay, Z. Su, B. Kapusuzoglu, Discrete eigenseparation-based reduced order homogenization method for failure modeling of composite materials, Computer Methods in Applied Mechanics and Engineering 359 (2020) 112656.
[64] D. R. Brandyberry, X. Zhang, P. H. Geubelle, A gfem-based reduced-order homogenization model for heterogeneous materials under volumetric and interfacial damage, Computer Methods in Applied Mechanics and Engineering 377 (2021) 113690.
[65] D. Xia, C. Oskay, Reduced order mathematical homogenization method for polycrystalline microstructure with microstructurally small cracks, International Journal for Numerical Methods in Engineering 124 (2023) 3166–3190.
[66] X. Zhang, Y. Liu, C. Oskay, Multiscale reduced-order modeling of a titanium skin panel subjected to thermomechanical loading, AIAA Journal 60 (1) (2022) 302–315.
[67] F. Meissonnier, E. Busso, N. O'Dowd, Finite element implementation of a generalised non-local rate-dependent crystallographic formulation for finite strains, International Journal of Plasticity 17 (4) (2001) 601–640.
[68] E. Marin, P. Dawson, On modelling the elasto-viscoplastic response of metals using polycrystal plasticity, Computer Methods in Applied Mechanics and Engineering 165 (1-4) (1998) 1–21.
[69] W. Liu, A. Tang, D. Ye, Z. Ji, Nonnegative singular value decomposition for microarray data analysis of spermatogenesis, in: 2008 International Conference on Information Technology and Applications in Biomedicine, IEEE, 2008, pp. 225–228.
[70] R. Hettich, K. O. Kortanek, Semi-infinite programming: theory, methods, and applications, SIAM Review 35 (3) (1993) 380–429.
[71] J. Hernández, J. Oliver, A. E. Huespe, M. Caicedo, J. Cante, High-performance model reduction techniques in computational multiscale homogenization, Computer Methods in Applied Mechanics and Engineering 276 (2014) 149–189.
[72] J. A. Hernandez, M. A. Caicedo, A. Ferrer, Dimensional hyper-reduction of nonlinear finite element models via empirical cubature, Computer Methods in Applied Mechanics and Engineering 313 (2017) 687–722.
[73] J. Yvonnet, Q. He, The reduced model multiscale method (r3m) for the non-linear homogenization of hyperelastic media at finite strains, Journal of Computational Physics 223 (1) (2007) 341–368.
[74] T. Bui-Thanh, K. Willcox, O. Ghattas, Model reduction for large-scale systems with high-dimensional parametric input space, SIAM Journal on Scientific Computing 30 (6) (2008) 3270–3288.
[75] K. Carlberg, C. Farhat, A low-cost, goal-oriented 'compact proper orthogonal decomposition' basis for model reduction of static systems, International Journal for Numerical Methods in Engineering 86 (3) (2011) 381–402.
[76] R. Quey, M. Kasemer, The neper/fepx project: free/open-source polycrystal generation, deformation simulation, and post-processing, in: IOP Conference Series: Materials Science and Engineering, Vol. 1249, IOP Publishing, 2022, p. 012021.
[77] C. Geuzaine, J.-F. Remacle, Gmsh: a 3-d finite element mesh generator with built-in pre-and post-processing facilities, International Journal for Numerical Methods in Engineering 79 (11) (2009) 1309–1331.
[78] V. Chiaruttini, V. Riolo, F. Feyel, Advanced remeshing techniques for complex 3d crack propagation, Icf13 (2013) 547–555.
[79] W. Aquino, J. Brigham, C. Earls, N. Sukumar, Generalized finite element method using proper orthogonal decomposition, International Journal for Numerical Methods in Engineering 79 (7) (2009) 887–906.
[80] A. Radermacher, S. Reese, Model reduction in elastoplasticity: proper orthogonal decomposition combined with adaptive sub-structuring, Computational Mechanics 54 (3) (2014) 677–687.
[81] P. M. L. Tammes, On the origin of number and arrangement of the places of exit on the surface of pollen-grains, Recueil des Travaux Botaniques néerlandais 27 (1) (1930) 1–84.
[82] J. J. Thomson, Xxiv. on the structure of the atom: an investigation of the stability and periods of oscillation of a number of corpuscles arranged at equal intervals around the circumference of a circle; with application of the results to the theory of atomic structure, The London, Edinburgh, and Dublin Philosophical Magazine and Journal of Science 7 (39) (1904) 237–265.
[83] E. A. Rakhmanov, E. Saff, Y. Zhou, Electrons on the sphere, in: Computational Methods and Function Theory 1994, World Scientific, 1995,

pp. 293–309.
[84] P. Bourke, Circles and spheres, Paul Bourke (1992).
[85] C. Hüttig, K. Stemmer, The spiral grid: a new approach to discretize the sphere and its application to mantle convection, Geochemistry, Geophysics, Geosystems 9 (2) (2008).
[86] T. W. M. Team, Evenly distributed points on sphere.
URL http://web.archive.org/web/20120421191837/http://www.cgafaq.info/wiki/Evenly$_{\text{d}}$istributed$_{\text{p}}$o
ints$_{\text{o}}$n$_{\text{s}}$phere
[87] M. Lin, Uniform-orientation-sampling.
URL https://github.com/M-Lin-DM/Uniform-Orientation-Sampling
[88] M. J. Powell, A direct search optimization method that models the objective and constraint functions by linear interpolation, in: Advances in Optimization and Numerical Analysis, Springer, 1994, pp. 51–67.
[89] S. G. Johnson, The nlopt nonlinear-optimization package.
URL http://github.com/stevengj/nlopt
[90] M. E. Wall, A. Rechtsteiner, L. M. Rocha, Singular value decomposition and principal component analysis, in: A practical approach to microarray data analysis, Springer, 2003, pp. 91–109.
[91] J. L. Chaboche, S. Kruch, J. F. Maire, T. Pottier, Towards a micromechanics based inelastic and damage modeling of composites, International Journal of Plasticity 17 (4) (2001) 411–439.
[92] J. Fish, V. Filonova, Z. Yuan, Hybrid impotent–incompatible eigenstrain based homogenization, International Journal for Numerical Methods in Engineering 95 (1) (2013) 1–32.